

RESEARCH ARTICLE | SEPTEMBER 22 2022

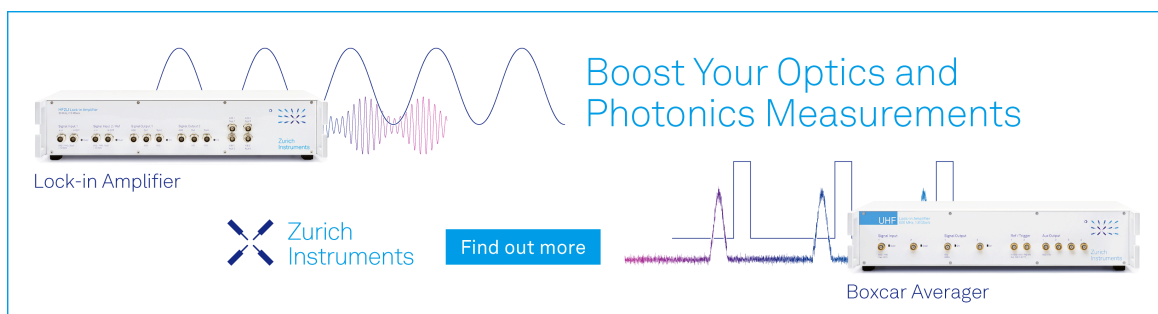
## Interfacial properties of binary azeotropic mixtures of simple fluids: Molecular dynamics simulation and density gradient theory

Jens Staubach; Simon Stephan  




*J. Chem. Phys.* 157, 124702 (2022)

<https://doi.org/10.1063/5.0100728>



Boost Your Optics and  
Photonics Measurements

Lock-in Amplifier

 Zurich  
Instruments

[Find out more](#)

Boxcar Averager

# Interfacial properties of binary azeotropic mixtures of simple fluids: Molecular dynamics simulation and density gradient theory

Cite as: J. Chem. Phys. 157, 124702 (2022); doi: 10.1063/5.0100728

Submitted: 26 May 2022 • Accepted: 11 July 2022 •

Published Online: 22 September 2022



View Online



Export Citation



CrossMark

Jens Staubach and Simon Stephan<sup>a)</sup> 

## AFFILIATIONS

Laboratory of Engineering Thermodynamics (LTD), TU Kaiserslautern, 67663 Kaiserslautern, Germany

<sup>a)</sup> Author to whom correspondence should be addressed: [Simon.Stephan@mv.uni-kl.de](mailto:Simon.Stephan@mv.uni-kl.de)

## ABSTRACT

Interfacial properties of binary azeotropic mixtures of Lennard-Jones truncated and shifted fluids were studied by molecular dynamics (MD) simulation and density gradient theory (DGT) in combination with an equation of state. Three binary mixtures were investigated, which differ in the energetic cross interaction parameter that yields different types of azeotropic behavior. This study covers a wide temperature and composition range. Mixture A exhibits a heteroazeotrope at low temperatures, which changes to a low-boiling azeotrope at high temperatures, mixture B exhibits a low-boiling azeotrope, and mixture C exhibits a high-boiling azeotrope. The phase behavior and fluid interfacial properties as well as their relation were studied. Vapor–liquid, liquid–liquid, and vapor–liquid–liquid equilibria and interfaces were considered. Density profiles, the surface tension, the interfacial thickness, as well as the relative adsorption and enrichment of the components at the interface were studied. The results obtained from the two independent methods (MD and DGT) are overall in good agreement. The results provide insights into the relation of the phase behavior, particularly the azeotropic behavior, of simple fluid mixtures and the corresponding interfacial properties. Strong enrichment was found for the mixture with a heteroazeotrope in the vicinity of the three-phase equilibrium, which is related to a wetting transition.

© 2022 Author(s). All article content, except where otherwise noted, is licensed under a Creative Commons Attribution (CC BY) license (<http://creativecommons.org/licenses/by/4.0/>). <https://doi.org/10.1063/5.0100728>

## I. INTRODUCTION

Phase equilibria and interfacial properties of fluids play an important role in many industrial processes and nature. This includes environmental science, process engineering, and energy technology. While data from laboratory experiments are readily available for phase equilibria for a large number of pure substances and mixtures, experimental data for interfacial properties are scarce. Since the thickness of both vapor–liquid and liquid–liquid interfaces lies on the nanoscale, it is practically impossible to study density and pressure profiles across fluid interfaces in laboratory experiments. Such nanoscopic properties can, however, be determined by computational methods based on molecular thermodynamics, e.g., molecular simulation and density gradient theory (DGT).

Interesting phenomena can be observed at fluid interfaces of mixtures: individual component density profiles can exhibit a

maximum in the interfacial region between the two bulk phases. This phenomenon is frequently observed for vapor–liquid interfaces.<sup>1</sup> This maximum can reach values several times higher than the corresponding bulk phase values. This phenomenon is called *enrichment*.<sup>1</sup> In particular, the enrichment at fluid interfaces is suspected to inhibit the mass transfer through interfaces.<sup>2–6</sup> It was found that wide-boiling phase behavior favors the enrichment, e.g., binary mixtures with a supercritical component. Ideal mixtures, on the contrary, usually show no enrichment. An enrichment is usually only observed for the low-boiling component.<sup>1</sup> Mixtures with azeotropic phase behavior are interesting regarding the enrichment behavior since components may change their roles of being high-boiling and low-boiling components at the azeotropic point. The enrichment was found to be strongly temperature dependent: it decreases with increasing temperature.<sup>1,7</sup> In addition, a direct relation between the enrichment and the wetting behavior at vapor–liquid–liquid equilibria has been elucidated.<sup>6–8</sup> Fluid

interfacial properties of azeotropic and heteroazeotropic systems have been studied only a few times using methods from molecular thermodynamics.<sup>6,9–13</sup> In particular, no comprehensive evaluation of the enrichment behavior in azeotropic systems is yet available.

Azeotropes are points in the phase diagram, where the composition of vapor and liquid phases in equilibrium is equal. Azeotropic behavior is practically highly relevant and of prime importance for distillation processes. Azeotropes usually form when two components have similar vapor pressure curves and the cross interactions differ from the pure component interactions. Attractive cross interactions between two components of a binary mixture result in a high-boiling azeotrope, i.e., the azeotrope has a higher boiling temperature than either of the pure components; in contrast, weak attractive cross interactions between two components result in a low-boiling azeotrope, i.e., the azeotrope has a lower boiling temperature than either of the pure components. Low-boiling azeotropic behavior occurs far more often than high-boiling azeotropic behavior.<sup>14,15</sup> For very weak attractive cross interactions, liquid–liquid demixing may occur in conjunction with an azeotrope leading to a heteroazeotrope (which is always low-boiling). Under heteroazeotropic conditions, a three-phase vapor–liquid–liquid equilibrium (VLE) occurs. For both high-boiling and low-boiling azeotropic behavior, the locus of azeotropic points constitutes the so-called azeotropic line—usually considered in the  $pTx$  space. The thermodynamic properties—especially the composition—of the interphase at azeotropic conditions have not yet been systematically studied. For a binary mixture, the azeotropic line separates two vapor–liquid equilibrium composition regions: one region spanning from the first pure component to the azeotropic line and the second region spanning from the azeotropic line to the second pure component. Moreover, azeotropic mixtures are known for a long time to exhibit an interesting behavior of the surface tension:<sup>16</sup> the surface tension isotherms of low-boiling/high-boiling azeotropic binary mixtures usually exhibit a minimum/maximum, respectively, as a function of the composition, which is directly linked to the composition of the interphase via the Gibbs adsorption equation. This surface tension extremum phenomenon is usually referred to as “aneotropy.”<sup>6,17</sup> Yet, the nanoscopic structure of this phenomenon is not yet fully understood.

The azeotropic point of a mixture is at times referred to as a “pseudo-pure component”<sup>13,15,18</sup> due to the fact that, in addition to the phase equilibrium conditions (equal pressure, temperature, and chemical potential), also the composition of the two phases is equal. Hence, a high-boiling azeotropic point can be considered as a high-boiling pseudo-pure component in the two phase equilibrium regions and a low-boiling azeotropic point as a low-boiling pseudo-pure component. No systematic investigation has yet been carried out on the nanoscopic interfacial properties at state points on the azeotropic line.

Yet, interfacial properties of azeotropic mixtures have been studied by computational methods in the literature at times.<sup>6,9–11,13</sup> Fouad and Vega<sup>9</sup> used DGT to study mixtures of refrigerants exhibiting low-boiling azeotropic behavior focusing on the aneotropy. Telo da Gama and Evans<sup>6</sup> studied the phase equilibria and interfacial properties upon the transition from homogeneous azeotropic behavior to heteroazeotropic behavior of a Lennard-Jones mixture using DGT. Schäfer *et al.*<sup>10</sup> studied vapor–liquid interfacial properties and the phase equilibria of binary

dimethylformamide + n-alkane mixtures, which exhibit low-boiling azeotropic behavior at moderate and high temperatures and heteroazeotropic behavior at low temperatures. Schäfer *et al.*<sup>10</sup> found that, depending on the location in the phase diagram, either dimethylformamide or the alkane component may exhibit an enrichment at the interface. González-Barramuño *et al.*<sup>13</sup> recently studied various azeotropic mixtures using both molecular dynamics (MD) simulations and DGT and found an azeotropic behavior with a surface tension minimum for all considered mixtures. Moreover, they have discussed the applicability of a “pseudo-pure component” concept for describing azeotropic conditions.<sup>13</sup> We have recently carried out a systematic study on the vapor–liquid interfacial properties of binary Lennard-Jones mixtures using both MD simulations and DGT.<sup>11</sup> The studied systems included one system with a low-boiling azeotrope and one system with a high-boiling azeotrope. Yet, the systems were only studied at a single temperature. Under these conditions, a significant enrichment of the low-boiling component was found for the mixture with a low-boiling azeotrope.

In this work, we have carried out MD simulations and DGT calculations in combination with an equation of state (EOS) to study planar vapor–liquid, liquid–liquid, and vapor–liquid–liquid interfaces of three azeotropic systems of simple fluid mixtures. This study was carried out using the Lennard-Jones truncated and shifted (LJTS) potential with a cutoff radius of  $2.5\sigma$ . This model system has been systematically studied in recent years regarding phase equilibrium properties,<sup>19,20</sup> interfacial properties,<sup>7,11</sup> and transport properties<sup>21</sup> for both the pure LJTS substance and LJTS mixtures. Here, we have studied three binary LJTS systems: one system with a heteroazeotrope and two systems with a homogeneous azeotrope. The three systems were studied in the entire temperature range where fluid phase equilibria exist. The focus of this work lies on the relation of azeotropic phase behavior and the fluid interfacial properties of the binary mixtures.

## II. MODELING AND SIMULATION

### A. Binary mixtures of Lennard-Jones truncated and shifted fluids

The Lennard-Jones truncated and shifted (LJTS) potential is highly efficient as it provides a good compromise of required computational effort and physical modeling depth. Moreover, the LJTS potential gives a realistic description of simple real fluids<sup>22</sup> and is frequently used in conceptual studies.<sup>23–26</sup> The LJTS potential  $u_{LJTS}$  is defined as

$$u_{LJTS}(r) = \begin{cases} u_{LJ}(r) - u_{LJ}(r_c), & r \leq r_c, \\ 0, & r > r_c, \end{cases} \quad (1)$$

and

$$u_{LJ}(r) = 4\epsilon \left[ \left( \frac{\sigma}{r} \right)^{12} - \left( \frac{\sigma}{r} \right)^6 \right], \quad (2)$$

with the energy and size parameter  $\epsilon$  and  $\sigma$ , respectively, the distance between two particles  $r$ , and the cutoff radius  $r_c = 2.5\sigma$ . Throughout

this work, all physical properties are reduced using the Lennard-Jones potential parameters  $\varepsilon$  and  $\sigma$ , the molecular mass  $M$  of the high-boiling component, and the Boltzmann constant  $k_B$ .<sup>27</sup>

In this work, we have studied three different binary LJTS mixtures labeled A, B, and C. The binary mixtures consist of two components: component 1 is the high-boiling component and component 2 is the low-boiling component. All three mixtures consist of the same pure component 1 and the same pure component 2. Component 1 is chosen as the reference component, i.e., all parameters are normalized using its size parameter  $\sigma_1$  and energy parameter  $\varepsilon_1$ .<sup>27</sup> Component 2 has a reduced energy parameter of  $\varepsilon_2 = 0.9\varepsilon_1$ . The size parameter of the two components is equal  $\sigma_1 = \sigma_2$ . For the calculation of the binary cross interaction parameters  $\sigma_{12}$  and  $\varepsilon_{12}$ , the modified Lorentz–Berthelot combination rules<sup>28,29</sup> were used:

$$\sigma_{12} = \frac{\sigma_1 + \sigma_2}{2}, \quad (3)$$

$$\varepsilon_{12} = \xi_{12} \sqrt{\varepsilon_1 \varepsilon_2}. \quad (4)$$

In Eq. (4),  $\xi_{12}$  is a state-independent cross interaction parameter. By varying  $\xi_{12}$ , the three following binary mixtures are obtained:

- mixture A with  $\xi_{12} = 0.8$ ,
- mixture B with  $\xi_{12} = 0.9$ , and
- mixture C with  $\xi_{12} = 1.2$ .

Each of the three mixtures was studied at six temperatures. The temperatures were chosen in such a way that for each mixture all characteristic phase equilibria were considered in the study. In a first step, the phase behavior of the three mixtures was computed using the PeTS (perturbed truncated and shifted) EOS, which is known to give an excellent description of binary LJTS mixtures.<sup>11,30</sup> This was done in a wide temperature and pressure range. The following temperatures were chosen for studying the interfacial properties: all three systems were studied at  $T = 0.77 \varepsilon k_B^{-1}$ ,  $0.88 \varepsilon k_B^{-1}$ , and  $0.99 \varepsilon k_B^{-1}$ . Depending on the system, three additional temperatures were considered:  $T = 0.715 \varepsilon k_B^{-1}$ ,  $0.825 \varepsilon k_B^{-1}$ , and  $0.935 \varepsilon k_B^{-1}$  for mixtures A and B and  $T = 0.66 \varepsilon k_B^{-1}$ ,  $1.06 \varepsilon k_B^{-1}$ , and  $1.12 \varepsilon k_B^{-1}$  for mixture C. The lowest temperature was chosen slightly above the triple point (TP) temperature of component 1 ( $T_1^{\text{TP}} = 0.65 \varepsilon k_B^{-1}$ ).<sup>31</sup> The highest considered temperature was chosen such that all types vapor–liquid phase equilibria were covered.

Mixture A exhibits a heteroazeotropic phase behavior, mixture B exhibits a low-boiling azeotropic behavior, and mixture C exhibits a high-boiling behavior. These three types of phase behavior are of very high practical relevance, which are common in industrial applications:<sup>14</sup> examples for heteroazeotropic behavior are acetonitrile + n-butane and water + 1-pentanol, examples for low-boiling azeotropic behavior are water + ethanol and methanol + acetone, and examples for low-boiling azeotropic behavior are ethane + CO<sub>2</sub> and water + formic acid.

## B. Molecular simulations

The MD simulations were carried out with the code *ls1 mardyn*<sup>32</sup> in the NVT ensemble with  $N = 16\,000$  particles. The simulation box contained a liquid slab in the middle surrounded

by two vapor slabs on each side. Periodic boundary conditions were applied in all directions of the box. Thereby, two rectangular and planar interfaces between the two phases were obtained, perpendicular to the  $z$ -axis of the box. From each simulation, the following quantities were sampled: the densities  $\rho''$  and  $\rho'$ , the composition vectors  $\underline{x}''$  and  $\underline{x}'$  of the vapor phase and liquid phase indicated by '' and ', respectively, the pressure in the bulk phases, and the interfacial properties surface tension  $\gamma$ , relative adsorption  $\Gamma$ , enrichment  $E$ , and interfacial thickness  $L_{90}^{10}$  (the definitions of the interfacial properties are given below). For all sampled quantities, the statistical uncertainty was estimated to be twice the standard deviation of the sampled block average values. Details on the MD simulations are given in the [supplementary material](#).

## C. PeTS EOS and density gradient theory

### 1. PeTS EOS

For the modeling of binary mixtures of the LJTS fluid, the PeTS EOS<sup>19</sup> was used. The parameters of the PeTS EOS were optimized for describing phase equilibrium and interfacial properties of the pure LJTS fluid. Hence, it gives an accurate description of such properties.<sup>19,33</sup> The PeTS EOS has been extended to mixtures<sup>11</sup> using the van der Waals one-fluid theory.<sup>34,35</sup> Despite the fact that the PeTS EOS was not parameterized for describing mixtures and corresponding results are accordingly predictions, the PeTS EOS gives an excellent description of both phase equilibrium and interfacial properties of mixtures as well.<sup>7,11,20,36</sup> In particular, the PeTS EOS exhibits a single van der Waals loop in the metastable/unstable region,<sup>19</sup> which makes it applicable in DGT for the modeling of interfacial properties. As expected, systematic deviations of molecular simulation results and results of the PeTS EOS have been reported in the vicinity of the critical point (CP),<sup>7,11</sup> which is due to the classical scaling behavior of the EOS.<sup>37–39</sup> The non-classical convergence in the vicinity of critical points could, in general, be incorporated into the EOS by a crossover term.<sup>40,41</sup> This would, however, result in additional numerical challenges<sup>40</sup> and is out of the scope of this work. The PeTS EOS is formulated in terms of the Helmholtz energy based on the perturbation theory of Barker and Henderson.<sup>42,43</sup> The mathematical structure of the PeTS EOS follows the structure of the monomer term of the PC-SAFT (perturbed-chain statistical associating fluid theory) EOS proposed by Gross and Sadowski,<sup>44</sup> which has been recently analyzed in detail.<sup>45</sup> The Helmholtz energy of the PeTS EOS is split into an ideal gas contribution  $a_{\text{id}}$ , a hard sphere contribution  $a_{\text{hs}}$  modeling the repulsive interactions, and a perturbation contribution  $a_{\text{pert}}$  modeling dispersive interactions. The Helmholtz energy per particle of the PeTS EOS is, therefore, written as

$$a = a_{\text{id}} + a_{\text{hs}} + a_{\text{pert}}, \quad (5)$$

which is a function of the temperature  $T$ , the total density of the mixture  $\rho$ , and the mole fraction vector of all components  $\underline{x}$ .

### 2. Density gradient theory

Density gradient theory in combination with an EOS is a frequently applied method for modeling interfacial properties of

fluids.<sup>46–48</sup> It is based on the pioneering work of van der Waals<sup>49</sup> and was modernized by Cahn and Hilliard.<sup>50</sup> In the following, only a brief introduction of the DGT framework is given. For a detailed description of the DGT, the reader is referred to the paper of Miquieu *et al.*<sup>51</sup> Details on the applied computational methods are given in the [supplementary material](#).

The DGT describes the Helmholtz energy of a heterogeneous domain, where two bulk phases are in contact at an interface. The Helmholtz energy is modeled by a second-order Taylor series approximation with respect to the component densities  $\rho_i$  for the components  $i = 1, 2$ . The Helmholtz energy density  $\hat{a} = a/V$  for the interface is then calculated as

$$\hat{a}[\underline{\rho}] = \hat{a}_0(\underline{\rho}) + \sum_{i=1}^2 \sum_{j=1}^2 \frac{1}{2} \kappa_{ij} \nabla \rho_i \nabla \rho_j, \quad (6)$$

where  $\hat{a}_0$  is the Helmholtz energy density of the phases in equilibrium,  $\nabla \rho_i$  and  $\nabla \rho_j$  are the local gradients of the component densities,  $\kappa_{ij}$  denote the influence parameters, and  $\underline{\rho}$  is the vector of number densities of the components. The pure component influence parameters are denoted by  $\kappa_{ii}$  and the cross interaction influence parameter by  $\kappa_{ij}$ .

The influence parameter of reference component 1  $\kappa_1$  was adopted from the work of Heier *et al.*<sup>19</sup> as  $\kappa_1 = 2.7334 \text{ \AA} \sigma^5$ . The influence parameter of component 2  $\kappa_2$  was calculated as  $\kappa_2 = \kappa_1 \frac{\epsilon_2}{\epsilon_1}$ . The cross interaction influence parameter  $\kappa_{12}$  was calculated using the geometric mixing rule

$$\kappa_{12} = \sqrt{\kappa_1 \kappa_2}. \quad (7)$$

Applying geometric mixing for the modeling of the cross interaction influence parameter is well-established in the literature and was shown to lead to excellent agreement with computer experimental results for the interfacial properties.<sup>7,9,46,52–54</sup> Yet, there is no physical justification for Eq. (7).

#### D. Definition of interfacial properties

Density profiles and pressure profiles were obtained from both MD simulations and DGT as a function of the coordinate  $z$ , which is orthogonal to the planar interface. From these profiles, different interfacial properties were computed, namely, the surface tension, the relative adsorption, the interfacial enrichment, and the interfacial thickness. For DGT, the surface tension  $\gamma$  was computed from the density profiles as<sup>55</sup>

$$\gamma = \int \sum_{i=1}^2 \sum_{j=1}^2 \frac{1}{2} \kappa_{ij} \nabla \rho_i \nabla \rho_j dz. \quad (8)$$

The integration was carried out numerically. For MD, the surface tension was computed via the mechanical route<sup>56,57</sup>

$$\gamma = \frac{1}{2} \int_{-\infty}^{+\infty} (p_N - p_T) dz, \quad (9)$$

where  $p_N$  indicates the normal pressure, i.e., the  $z$ -component of the pressure tensor and  $p_T$  indicates the tangential pressure components. The tangential pressure was determined by averaging over the pressure components parallel to the interfacial area  $S$ . The interfacial area of each planar interface is given by the cross section of the simulation volume normal to the  $z$ -axis.

The relative adsorption of component  $i$  at the interface with respect to component  $j$  was calculated from the density profiles according to Telo da Gama and Evans<sup>6</sup> as

$$\Gamma_i^{(j)} = -(\rho_i' - \rho_i'') \int_{-\infty}^{+\infty} \left[ \frac{\rho_j(z) - \rho_j'}{\rho_j' - \rho_j''} - \frac{\rho_i(z) - \rho_i'}{\rho_i' - \rho_i''} \right] dz, \quad (10)$$

with  $i, j = 1, 2$  and  $i \neq j$ ,

where  $\rho_i', \rho_i''$  and  $\rho_j', \rho_j''$  are the bulk densities of the liquid phase ' and vapor phase ''. The integration was carried out numerically. In general, a positive value of the relative adsorption  $\Gamma_i^{(j)}$  of component  $i$  with respect to component  $j$  can be the result of an enrichment of component  $i$  or a relative shift of the two component density profiles  $i$  and  $j$ .<sup>11,20</sup>

The enrichment  $E_i$  is a second quantity for characterizing the interfacial excess of component  $i$ .<sup>1</sup> The enrichment  $E_i$  is defined as<sup>58</sup>

$$E_i = \frac{\max(\rho_i(z))}{\max(\rho_i', \rho_i'')} \quad \text{with } i = 1, 2. \quad (11)$$

The numerator indicates the maximum of the density profile  $\rho_i(z)$ . The denominator indicates the maximum of the two bulk phase densities  $\rho_i', \rho_i''$ . For the MD simulation results, the density profiles exhibit some random noise, which leads to indistinguishable results for values of  $E_i < 1.1$ , as discussed in previous studies.<sup>7,20</sup> This problem could, in general, be circumvented by adapting the definition of the enrichment.<sup>11</sup> We chose to keep the simple expression for the enrichment given by Eq. (11) in favor of reducing the (mostly negligible) artifacts for very small enrichment. The enrichment  $E_i$  can also be computed from the empirical enrichment model proposed by Stephan and Hasse<sup>1</sup> based on phase equilibrium data solely. This model was also applied in this work in conjunction with the PeTS EOS.

Moreover, the thickness of the fluid interfaces was studied. Here, we have applied the definition for the effective interfacial thickness  $L_{10}^{90}$  according to Lekner and Henderson.<sup>59</sup> It is defined as the distance in the  $z$ -direction between the points  $z(\rho_{10})$  and  $z(\rho_{90})$  of the density profile. Between these points, the total number density changes from  $\rho_{10} = \rho'' + 0.1(\rho' - \rho'')$  to  $\rho_{90} = \rho'' + 0.9(\rho' - \rho'')$  and the interfacial thickness can be calculated as

$$L_{10}^{90} = z(\rho_{90}) - z(\rho_{10}). \quad (12)$$

### III. RESULTS AND DISCUSSION

The numeric values obtained from MD and DGT + EOS for the phase equilibria and the interfacial properties for the three



systems are reported in the [supplementary material](#). In this section, first, the phase equilibria are discussed, and then the properties of the interfaces and their relation to the underlying phase equilibria are discussed. For the interfacial properties, first, results for the different two-phase regions (VLE and LLE) of the azeotropic mixtures are discussed; then, results along two characteristic lines are discussed: the azeotropic line and the VLLE line.

### A. Phase equilibria

The pressure–composition phase diagrams for the three mixtures at all studied temperatures are shown in [Figs. 1\(a\)–1\(c\)](#) [[Figs. 1\(a\)–1\(c\)](#) are presented in the [supplementary material](#) with all error bars shown]. The pressure–temperature projections with the

characteristic lines (pure component vapor–pressure curves, critical line, azeotropic line, and VLLE line) are shown in [Figs. 1\(d\)–1\(f\)](#). From top to bottom, the mixtures are arranged as mixture A, mixture B, and mixture C. Results from MD and the EOS are shown in the phase diagrams; only EOS results are shown in the pressure–temperature projection diagrams. Mixture A (top) and mixture B (middle) were studied at the same six temperatures. Mixture C (bottom) was also studied at six temperatures but differently chosen. Three of the temperatures considered for mixture C are identical to the studied temperatures for mixture A and mixture B ( $T = 0.77 \epsilon k_B^{-1}$ ,  $0.88 \epsilon k_B^{-1}$ , and  $0.99 \epsilon k_B^{-1}$ ). Mixture A and mixture B correspond to a type II-A system according to the classification of van Konynenburg and Scott,<sup>60</sup> while the phase behavior of mixture C is type I-A. For both type I-A and type II-A systems,

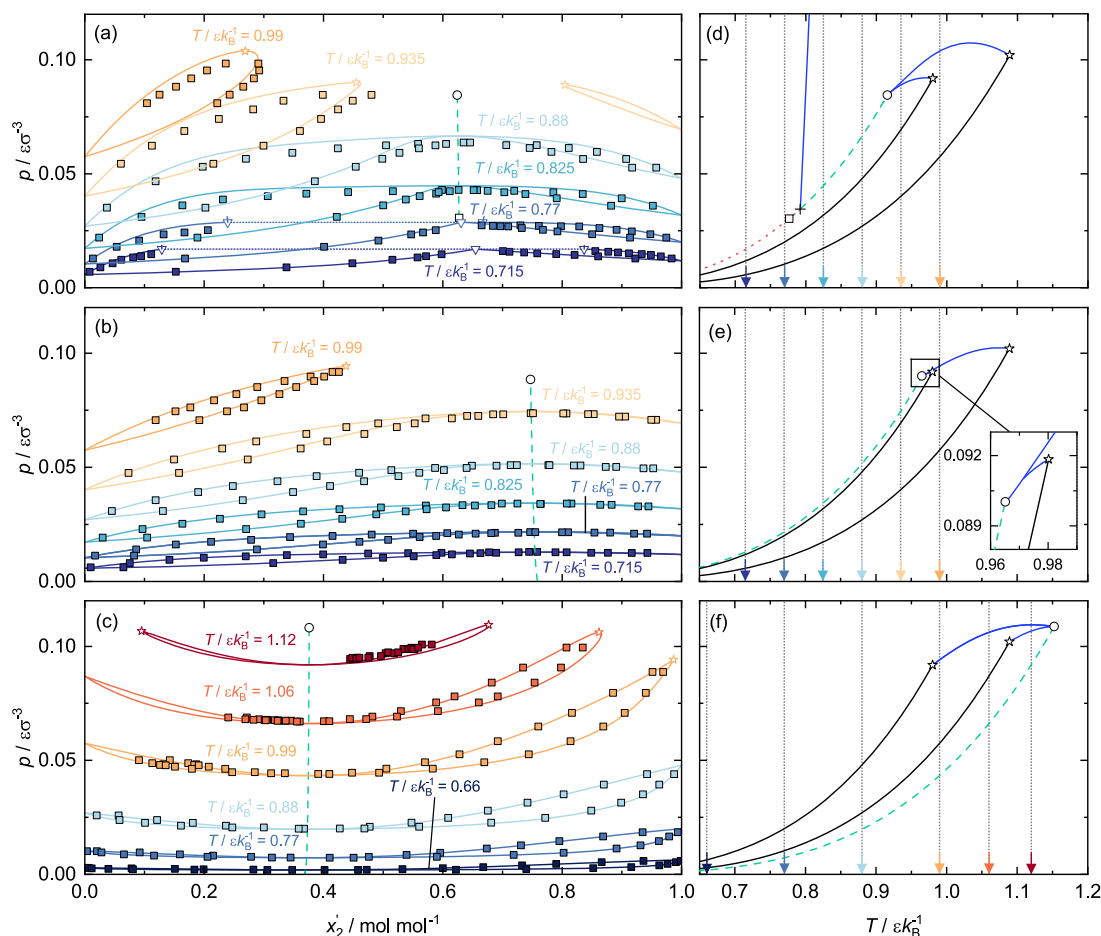


**FIG. 1.** Phase equilibria of the three studied binary LJTS mixtures. From top to bottom: mixture A, mixture B, and mixture C. Left: isothermal pressure–composition phase diagrams for different temperatures (color-coded). In addition, the azeotropic line (green dashed line), critical azeotropic endpoint (CAEP) ( $\circ$ ), and heteroazeotropic endpoint (HAEP) ( $\square$ ) are shown. Filled symbols are MD results and lines are PeTs EOS<sup>11,19</sup> results. Right: corresponding pressure–temperature projection diagrams for the EOS: critical lines (blue solid lines), azeotropic line (green dashed line), VLLE line (red dotted line), and the pure component vapor–pressure curves (black solid lines). Open symbols represent critical points ( $\star$ ), critical endpoint (CEP) ( $+$ ), critical azeotropic endpoint (CAEP) ( $\circ$ ), heteroazeotropic endpoint (HAEP) ( $\square$ ), and three-phase equilibrium (VLLE) ( $\nabla$ ) obtained from the EOS. The studied temperatures for each mixture are indicated by the vertical dashed lines and arrows. [Figures 1\(a\)–1\(c\)](#) that include error bars are presented in the [supplementary material](#).

the pure component critical points are connected by an uninterrupted critical line [cf. Figs. 1(d)–1(f)]. Type II-A systems exhibit an additional liquid–liquid critical line that ends in a critical endpoint (CEP). Numeric values of characteristic points, i.e., the critical point (CP), triple point (TP), critical endpoint (CEP), critical azeotropic endpoint (CAEP), and heteroazeotropic endpoint (HAEP), of the three mixtures are summarized in Table I.

The phase equilibrium results obtained from the independent predictions of MD and the EOS are overall in excellent agreement for all mixtures and studied temperatures [cf. Figs. 1(a)–1(c)]. Only in the direct vicinity of critical points, systematic deviations are observed. Such deviations are found at the two highest studied temperatures of mixture A [cf. Fig. 1(a)].

Mixture A exhibits two different types of azeotropic behavior depending on the temperature [cf. Fig. 1(d)]: a homogeneous low-boiling azeotrope is formed at temperatures above the temperature of the heteroazeotropic endpoint (HAEP) up to the temperature of the critical azeotropic endpoint (CAEP) (cf. Table I). The low-boiling azeotrope of mixture A turns into a heterogeneous azeotrope below the temperature of the HAEP. This transition is a consequence of the existing three-phase equilibrium (VLE) at low temperatures. For mixture A, at temperatures  $T < T_A^{\text{CEP}}$ , a three-phase VL<sub>1</sub>L<sub>2</sub> equilibrium occurs [dotted red line in Fig. 1(d)]. Moreover, in the temperature range  $T < T_A^{\text{CEP}}$ , three two-phase regions are attached to the three-phase equilibrium: an L<sub>1</sub>L<sub>2</sub> equilibrium region (not shown in Fig. 1 for clarity), a VL<sub>1</sub> equilibrium region, and a VL<sub>2</sub> equilibrium region. The phase L<sub>1</sub> indicates component 1-rich phase, whereas L<sub>2</sub> indicates component 2-rich phase. For mixture A, at  $T = T_A^{\text{CEP}}$ , the L<sub>1</sub>L<sub>2</sub> equilibrium region detaches with increasing temperature from the VLE regions, which goes in hand with the breakup of the heteroazeotrope. More isothermal

phase diagrams in the vicinity of  $T_A^{\text{HAEP}}$  and  $T_A^{\text{CEP}}$  are depicted in the supplementary material. The L<sub>1</sub>L<sub>2</sub> equilibrium region detaches upon the formation of a liquid–liquid critical point at  $T_A^{\text{CEP}}$ . Hence, the liquid–liquid critical line starts at  $T_A^{\text{CEP}}$  [cf. Fig. 1(f)]. In the temperature range  $T > T_A^{\text{CEP}}$ , one L<sub>1</sub>L<sub>2</sub> equilibrium region exists, which ends in a lower critical point, and two vapor–liquid equilibrium regions VL<sub>1</sub> and VL<sub>2</sub> exist, which are connected at the azeotropic line.

Mixture B has a similar phase behavior as mixture A, but the CEP (predicted from the EOS) is well below the triple point temperature of the pure component 1 (cf. Table I). Thus, no VLE is observed in the studied temperature region. Therefore, the azeotropic line of mixture B exists in a wide temperature range [cf. Fig. 1(e)]. At the critical azeotropic endpoint (CAEP), the two vapor–liquid equilibrium regions VL<sub>1</sub> and VL<sub>2</sub> connected by the azeotropic line break apart such that the vapor–liquid equilibrium regions are separated. This breaking up goes in hand with the occurrence of two critical points—one for each vapor–liquid equilibrium region. Therefore, the CAEP is a bi-critical point. All but one of the studied isothermal phase equilibria of mixture B exhibit a low-boiling azeotrope [cf. Fig. 1(b)]. The highest temperature shown in Fig. 1(b)  $T = 0.99 \text{ } \epsilon k_B^{-1}$  is above the temperature of the CAEP, i.e., no azeotropic point exists and the low-boiling component is supercritical.

Mixture C exhibits a high-boiling azeotrope in the entire studied temperature range [cf. Fig. 1(f)]. The two vapor–liquid equilibrium regions VL<sub>1</sub> and VL<sub>2</sub> are connected at the azeotropic line. The azeotropic line ends at a CAEP, where the two critical points of the two vapor–liquid equilibrium regions VL<sub>1</sub> and VL<sub>2</sub> merge into one bi-critical point. For the isothermal phase equilibrium at  $T = 1.06 \text{ } \epsilon k_B^{-1}$ , the low-boiling component 2 is supercritical,

**TABLE I.** Temperature  $T$ , pressure  $p$ , and mole fraction  $x_2$  of characteristic points of the pure components and the studied mixtures. The pure component critical point (CP) and the triple point (TP) are listed; results from both MD<sup>31,70</sup> and the PeTS EOS.<sup>19</sup> For the mixtures, the critical azeotropic endpoint (CAEP), the heteroazeotropic endpoint (HAEP), and the critical endpoint of the LLE (CEP) are given. For the mixtures, only results computed from the PeTS EOS are given. For the mixtures, the composition of the vapor phase V, the liquid phase L<sub>1</sub>, and the liquid phase L<sub>2</sub> are given—if applicable.

	$T/\epsilon k_B^{-1}$	$p/\epsilon \sigma^{-3}$	$x_2^V/\text{mol mol}^{-1}$	$x_2^{L_1}/\text{mol mol}^{-1}$	$x_2^{L_2}/\text{mol mol}^{-1}$
Pure substances					
CP (EOS)	1.089	0.102 0	...	...	...
CP (MD) <sup>70</sup>	1.0779	...	...	...	...
TP (MD) <sup>31</sup>	0.65	0.002 71	...	...	...
Mixture A					
CAEP (EOS)	0.916	0.084 6	0.626	0.626	...
HAEP (EOS)	0.776	0.030 3	0.627	0.264	0.627
CEP (EOS)	0.792	0.034 5	0.618	0.422	0.422
Mixture B					
CAEP (EOS)	0.965	0.090 0	0.744	0.744	...
Mixture C					
CAEP (EOS)	1.152	0.108 7	0.378	0.378	...

whereas the high-boiling component 1 is subcritical [cf. Fig. 1(c)]. At  $T = 1.12 \epsilon k_B^{-1}$ , both pure components are supercritical and each of the vapor–liquid equilibrium regions exhibits a critical point. This is due to the fact that the mixture exhibits higher mean dispersive interactions than the pure components, which yields a stable vapor–liquid equilibrium at temperatures higher than the two pure component critical temperatures.

Figure 2 shows the partition coefficients ( $K_i^{5\%} = x_i'' / x_i'$ ) of the two components  $i = 1, 2$  at a mole fraction of  $x_i' = 0.05 \text{ mol mol}^{-1}$  for the three studied mixtures as a function of the temperature. The partition coefficient at  $x_i' = 0.05 \text{ mol mol}^{-1}$  is used here to characterize the boiling behavior, which is known to be related to the enrichment behavior.<sup>1</sup> The partition coefficient is, therefore, used as the main descriptor in the empirical enrichment model of Ref. 1, which is also used for comparison below. Hence, it is interesting to compare the partition coefficient results predicted by the theory and those from computer experiments. Since the molecular simulations were not carried out at exactly  $x_i' = 0.05 \text{ mol mol}^{-1}$ , the MD results shown in Fig. 1 were interpolated between the two data points closest to that. Overall, the independent predictions from MD and the EOS for the partition coefficient are in very good agreement. The partition coefficient of component 2 is calculated at the liquid phase composition of  $x_2' = 0.05 \text{ mol mol}^{-1}$ , i.e.,  $K_2^{5\%} = x_2'' / 0.05 \text{ mol mol}^{-1}$ , and the partition coefficient of component 1 at a liquid phase composition of  $x_1' = 0.05 \text{ mol mol}^{-1}$ , i.e.,  $K_1^{5\%} = x_1'' / 0.05 \text{ mol mol}^{-1}$ . Hence, each of the two partition coefficients characterizes the boiling behavior in one of the vapor–liquid phase equilibrium regions (VL<sub>1</sub> and VL<sub>2</sub>) that are connected either by a heteroazeotropic point or an azeotropic point or are separated by two critical points (cf. Fig. 1). The partition coefficient  $K_2^{5\%}$  characterizes the vapor–liquid equilibrium region connected to the pure component 1, i.e., the VL<sub>1</sub> region, and  $K_1^{5\%}$  the vapor–liquid equilibrium region connected to the pure component 2, i.e., the VL<sub>2</sub> region. The partition coefficient  $K_2^{5\%}$  is in practically all cases larger than the partition coefficient  $K_1^{5\%}$ , which is simply due to the fact that

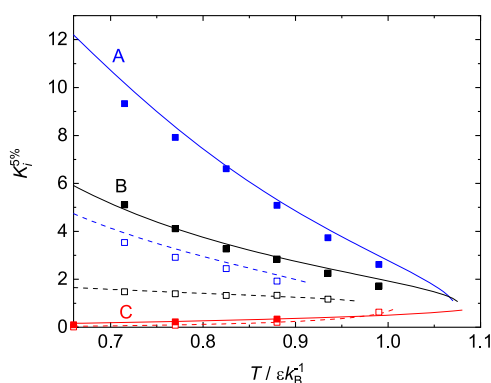


**FIG. 2.** Partition coefficient of component 1 (dashed lines and open squares) and component 2 (solid lines and filled squares) as a function of the temperature. Partition coefficients are given at liquid phase composition  $x_1' = 0.05 \text{ mol mol}^{-1}$  ( $K_1^{5\%}$ ) and  $x_2' = 0.95 \text{ mol mol}^{-1}$  ( $K_2^{5\%}$ ). Results for mixture A (blue), mixture B (black), and mixture C (red). Results from the PeTS EOS<sup>11,19</sup> (lines) and MD data (symbols).

component 2 is the overall low-boiling component and, therefore, has a stronger tendency to accumulate in the vapor phase. Moreover, this indicates that the VL<sub>1</sub> region connected to the high-boiling pure component 1 exhibits a wider boiling behavior than the VL<sub>2</sub> region connected to the low-boiling pure component 2. For mixture A and mixture B, the two partition coefficients are in the entire temperature range larger than unity. Hence, in each of the two vapor–liquid equilibrium regions VL<sub>1</sub> and VL<sub>2</sub>, the respective pure component effectively acts as the high-boiling component (until the azeotropic line). For mixture C on the other hand, both partition coefficients are  $K_1^{5\%} < 1$  and  $K_2^{5\%} < 1$  in the entire temperature range, which indicates that the particles have a preferential residency in the liquid phase of the other component. Hence, for mixture C, the pure components effectively act as the low-boiling component in the respective vapor–liquid equilibrium region (until the azeotropic point). Moreover, the comparison of the results for the three mixtures shows that, for a given temperature, the two considered partition coefficients decrease with increasing  $\xi_{12}$ , which is as expected: the attraction of particles of the two components increases with increasing  $\xi_{12}$ , which decreases the tendency that the two components partition into the two phases. Both partition coefficients  $K_1^{5\%}$  and  $K_2^{5\%}$  are found to strongly depend on the temperature (cf. Fig. 2). For mixture A and mixture B,  $K_2^{5\%}$  and  $K_1^{5\%}$  decrease with increasing temperature. On the contrary, for mixture C,  $K_2^{5\%}$  and  $K_1^{5\%}$  increase with increasing temperature. At high temperatures, the two partition coefficients for all three mixtures approach unity, which is due to the fact that attractive interactions become less dominant and the tendency of the two components to partition into two phases vanishes upon approaching a critical state.

## B. Interfacial properties

Figure 3 shows the density profiles of the VL<sub>1</sub> and VL<sub>2</sub> interface of all three studied mixtures at three temperatures obtained from DGT (the results for all other temperatures are presented in the [supplementary material](#)). The left column shows the results for mixture A, the middle column for mixture B, and the right column for mixture C. The corresponding plots for the MD results are presented in the [supplementary material](#). In addition, density profiles of the L<sub>1</sub>L<sub>2</sub> interface for mixture A for  $T = 0.715 \epsilon k_B^{-1}$  and  $T = 0.77 \epsilon k_B^{-1}$  are reported in the [supplementary material](#). It has been shown in earlier works of our group that the independent predictions from MD and DGT + PeTS EOS for the density profiles are in good agreement.<sup>4,11,33</sup> This is also supported by the good agreement of the interfacial properties derived from the density profiles obtained from the two methods and discussed in Sec. III B 1–III B 3.

Each plot shown in Fig. 3 corresponds to the results for one temperature for a given mixture. For each temperature and mixture, density profiles at 15 state points are shown. The density profiles of both the high-boiling and low-boiling components are shown as a function of the  $z$ -axis normal to the planar interface. The origin of the  $z$ -axis ( $z = 0$ ) was prescribed in all cases to the position  $\rho = \rho'' + 0.5(\rho' - \rho'')$ . The vapor–liquid interfaces at the azeotropic point (if existent at a given temperature) were explicitly computed by DGT, and the corresponding results are highlighted in Fig. 3, which also indicates the transition from the VL<sub>1</sub> equilibrium to the VL<sub>2</sub> equilibrium region.



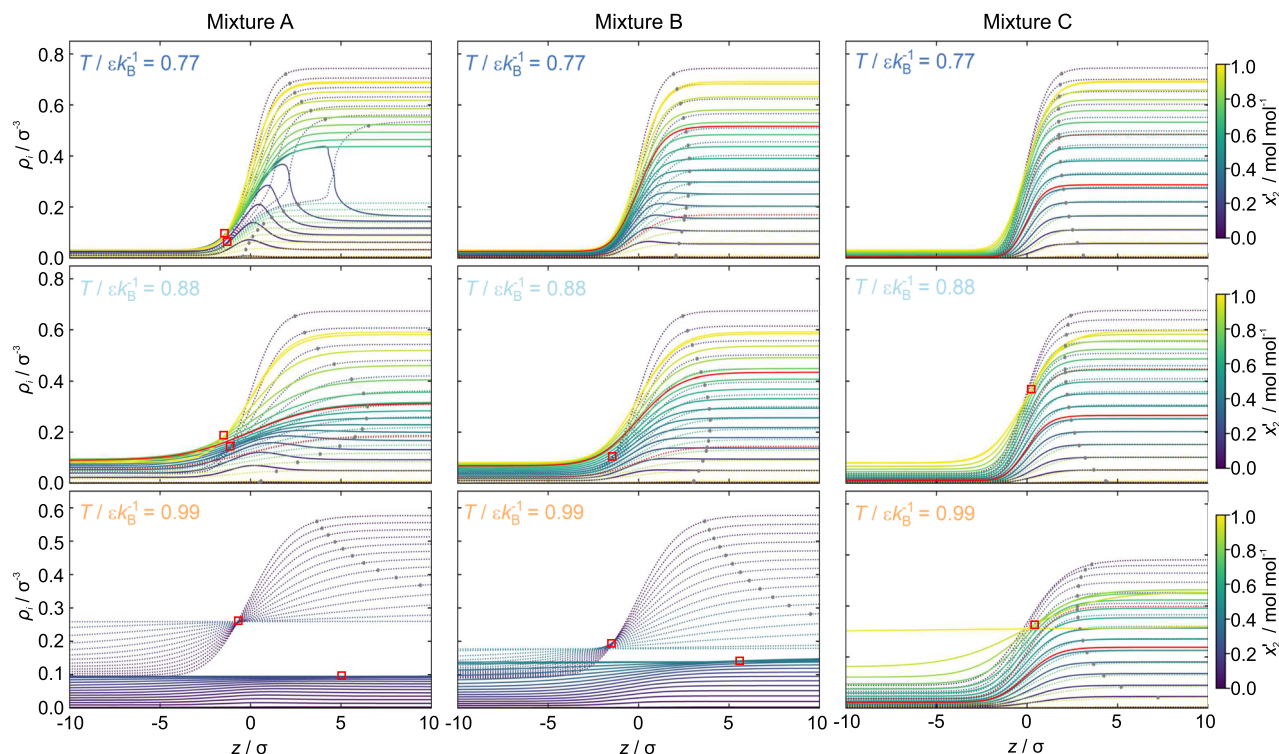


**FIG. 3.** Density profiles for the three studied mixtures obtained from DGT. Top to bottom corresponds to increasing temperature, as specified in each plot (the DGT density profiles for all other studied temperatures are presented in the [supplementary material](#)). Left: mixture A; middle: mixture B; right: mixture C. Dashed lines: high-boiling component 1; solid lines: low-boiling component 2. The color-code of the density profiles indicates the liquid phase concentration  $x_2^l$ . Red colored density profiles correspond to the azeotropic point density profiles at a given temperature. Gray dots indicate the  $z$ -coordinate, where the density of component 1 reaches 97% of the corresponding liquid bulk value. Invariant intersection points of multiple density profiles are indicated by red squares.

The density profiles of the three mixtures show important differences. For both, mixture A and mixture B, density profiles exhibit a distinct maximum between the two bulk phases. For mixture A and mixture B, the low-boiling component exhibits significant enrichment. Yet, only for mixture A, a faint enrichment of the high-boiling component is observed for some conditions (see also the [supplementary material](#)). With increasing temperature, this density maximum becomes less prominent before it vanishes. The density profiles for mixture C exhibit no maximum, i.e., all density profiles show a monotonic transition between the bulk phases at all studied conditions. Moreover, for mixture C, the interfaces of the mixture are narrower than the interfaces of the two pure components 1 and 2 at a given temperature. In contrast, the vapor–liquid interfaces of mixture A and mixture B are broadest in the vicinity of the azeotropic composition at a given temperature. This can be seen from the gray dots marking the position  $z_{1,97}$  at which the density profiles of component 1 reach 97% of the bulk liquid density (results for the 10–90 interfacial thickness computed from the density profiles are presented and discussed in the [supplementary material](#)). The density profiles of mixture A for the two lowest studied temperatures are strongly influenced by the occurrence of the VLLE (cf. [Fig. 3](#) and the [supplementary material](#)). For component 1's density profiles of the VL<sub>2</sub> interface, a small

density maximum builds up in the vicinity of the VLLE. For the density profiles of the VL<sub>1</sub> interface in the vicinity of the VLLE, the density maximum increases strongly and the interface is very broad. This is directly related to a wetting transition in the vicinity of the VLLE:<sup>8,11,61</sup> the liquid phase L<sub>2</sub> nucleates at the VL<sub>1</sub> interface under the influence of the gradients before the actual three-phase VLLE (cf. [Table I](#)) is established. This wetting transition is predicted in a very narrow pressure range of approximately  $0.0159\epsilon\sigma^{-3} < p < 0.0168\epsilon\sigma^{-3}$ . The corresponding composition range is between approximately  $0.105 \text{ mol mol}^{-1} < x_2^l < 0.129 \text{ mol mol}^{-1}$ .

For all studied mixtures, invariant intersection points are observed at several sets of isothermal density profiles (cf. [Fig. 3](#)). In these invariant intersection points, density profiles  $\rho_i(z)$  of component  $i$  approximately intersect at a given temperature. The occurrence of invariant intersection points in sets of fluid density profiles has already been reported before by Bongiorno and Davis<sup>62</sup> and Stephan *et al.*<sup>7,11,33,63</sup> Stephan and Hasse<sup>7</sup> discussed the relation between invariant intersection points in the density profiles and the corresponding phase diagram for two binary LJTS mixtures. A comprehensive discussion of the invariant intersection points observed in the density profiles of mixtures A, B, and C is given in the [supplementary material](#).

## 1. Surface tension

Figure 4 shows the results for the surface tension obtained from MD and DGT. The results from the two independent methods agree in practically all cases within the MD error bars. Only in the direct vicinity of the VLLE three-phase equilibrium, important deviations for the surface tension obtained from the two methods are observed. The corresponding DGT density profiles (cf. Fig. 3, top, left) exhibit extreme density gradients, which are due to the predicted wetting transition. The density (square) gradient theory, however, is only valid within the limit of low gradients.<sup>64</sup> Hence, the DGT VL<sub>1</sub> and VL<sub>2</sub> interface results in the vicinity of the VLLE should be interpreted with caution.

The low-boiling pure component 2 has a lower surface tension than the high-boiling component 1 at a given temperature. Since the three mixtures consist of the same pure components 1 and 2, the pure component limit values of a given surface tension isotherm are the same for all three mixtures (cf. Fig. 4). As expected, the surface tension goes to zero at critical points of the mixture.

The surface tension isotherms exhibit a minimum for mixture A and mixture B [cf. Figs. 4(a) and 4(b)], whereas the surface tension isotherms for mixture C exhibit a maximum [cf. Fig. 4(c)]. The minimum/maximum of the surface tension isotherms of the three mixtures is observed for all studied temperatures—also for those where one or both pure components are supercritical. The

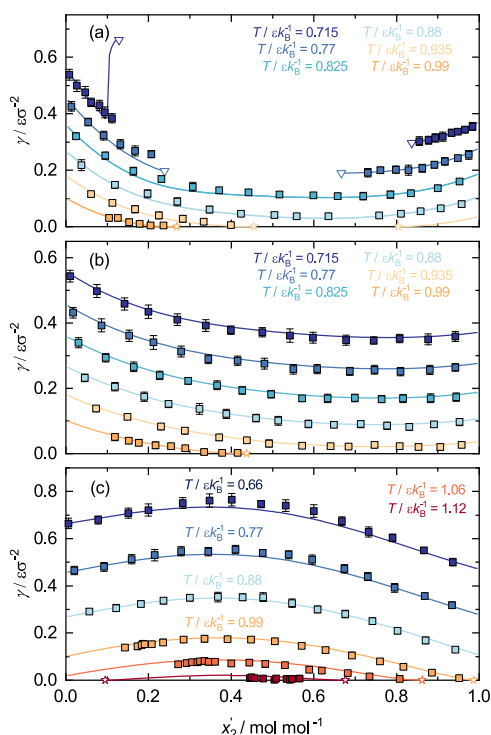


**FIG. 4.** Surface tension  $\gamma$  as a function of the liquid phase concentration  $x_2'$  for all studied temperatures and mixtures. Top to bottom are: mixture A, mixture B, and mixture C. Filled symbols represent data from MD simulations and lines predictions from DGT. Furthermore, the three-phase equilibrium ( $\nabla$ ) and the critical points ( $\star$ ) obtained from the EOS are indicated.

occurrence of a maximum in a surface tension isotherm is usually called positive aneutrope, whereas a minimum is usually called negative aneutrope.<sup>17</sup> The presence of a positive aneutrope comes along with a high-boiling azeotrope (mixture C). The presence of a negative aneutrope, on the other hand, comes along with a low-boiling azeotrope (mixture A and mixture B). Here, we use the conformal solution theory of Stephan and Hasse<sup>20</sup> to explain this behavior, which states that the mean liquid phase interactions dominate the vapor–liquid interfacial properties.<sup>20</sup> For the three studied mixtures, the liquid phase configurational internal energy can be described as a function of the cross interaction parameter  $\xi_{12}$ , the ratio of the dispersion energy  $\epsilon_1/\epsilon_2$ , and the liquid phase composition only.<sup>20</sup> For simple fluid mixtures, it was shown by Stephan and Hasse<sup>20</sup> that the interfacial tension increases with increasing liquid phase mean configurational internal energy. Here, the studied mixtures A, B, and C only differ in the cross interaction parameter  $\xi_{12}$ . Therefore, the configurational internal energy is only a function of  $\xi_{12}$  at constant liquid phase composition  $x'$ . Starting with  $\xi_{12} = 0.8$  (mixture A), the surface tension at a given temperature and liquid phase composition increases with increasing  $\xi_{12}$  ( $\xi_{12} = 0.9$  for mixture B and  $\xi_{12} = 1.2$  for mixture C) (cf. Fig. 4). The fact that surface tension isotherms pass a maximum or minimum can be explained by the interfacial conformal solution theory in a way that the cross interaction  $\xi_{12}$  parameter is most influential on the configurational internal energy for approximately equimolar compositions. Therefore, the difference in the value of the surface tension at a given temperature between mixture A, mixture B, and mixture C is the largest for approximately equimolar composition. In addition, for the compositions in the vicinity of the pure components, the surface tension difference between the mixtures has to vanish.

The occurrence of a VLLE for mixture A has an important influence on the surface tension isotherms [cf. Figs. 1(d) and 4(a)]. The negative aneutrope vanishes due to the miscibility gap. Therefore, the surface tension isotherm is split into two parts: the surface tension calculated for the VL<sub>1</sub> interface and for the VL<sub>2</sub> interface, respectively. For both branches, the lowest surface tension is found at the heteroazeotropic condition, i.e., at the VLLE. Yet, it should be noted that the VL<sub>1</sub> and VL<sub>2</sub> surface tension values at a given temperature at VLLE conditions [down triangles in Fig. 4(a)] are not equal. The interfacial properties along the VLLE line are discussed in more detail below. The surface tension at  $T = 0.715 \epsilon k_B^{-1}$  predicted by DGT increases strongly for the VL<sub>1</sub> interface in the direct vicinity of the VLLE, which is probably related to the extreme density gradients under these conditions.

## 2. Relative adsorption

Figure 5 shows the results for the relative adsorption of component 2 with respect to component 1 (Fig. 5 is presented in the supplementary material with all error bars shown). Results obtained from MD and DGT are shown. In addition, the results for the relative adsorption of component 1 with respect to component 2 are reported in the supplementary material. Overall, the agreement between the results from MD and DGT is good and in most cases within the MD error bars (see the supplementary material). Significant deviations between the results from the two methods are observed in the direct vicinity of the VLLE for mixture A.

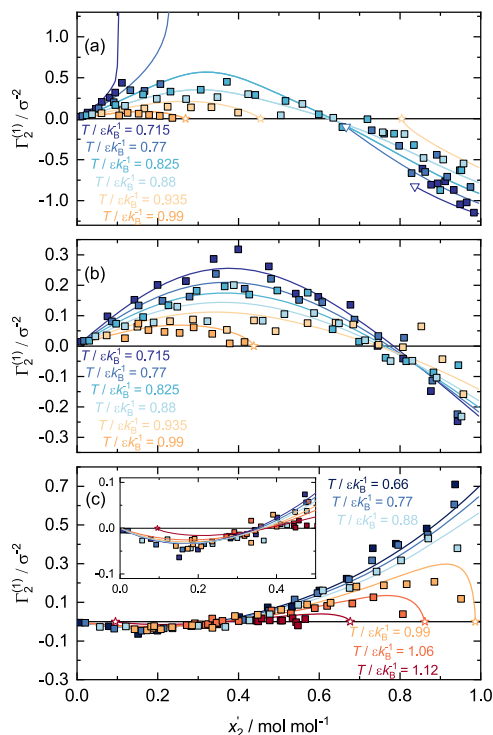


**FIG. 5.** Relative adsorption  $\Gamma_2^{(1)}$  as a function of the liquid phase concentration  $x_2'$  for all studied temperatures and mixtures. Top to bottom are: mixture A, mixture B, and mixture C. Filled symbols represent data from MD simulations and lines predictions from DGT. Furthermore, the three-phase equilibrium ( $\nabla$ ) and the critical points ( $*$ ) obtained from the EOS are indicated. Error bars are omitted for clarity. Figure 5 that includes error bars is presented in the [supplementary material](#).

For all three studied mixtures, the relative adsorption  $\Gamma_i^{(j)}$  of component  $i$  with respect to component  $j$  is zero for three types of conditions: infinite dilution of component  $i$ , an extremum in the surface tension isotherm (aneotrope), or a mixture critical point. Therefore, the adsorption isotherms of component 2 with respect to component 1  $\Gamma_2^{(1)}$  must exhibit an extremum between any two of these points [cf. Figs. 5(a)–5(c)]. This is also the case for the adsorption isotherms of component 1 with respect to component 2  $\Gamma_1^{(2)}$  (cf. Fig. S7 in the [supplementary material](#)). For mixture B, the adsorption isotherms of  $\Gamma_2^{(1)}$  and  $\Gamma_1^{(2)}$  yield a maximum in the VL<sub>1</sub> and VL<sub>2</sub> regions, respectively [cf. Fig. 5(b) and the [supplementary material](#)]. This is also the case for the adsorption isotherms for mixture A—excluding the temperatures, where a VLLE occurs ( $T = 0.715 \epsilon k_B^{-1}$ ,  $0.77 \epsilon k_B^{-1}$ ) [cf. Fig. 5(a) and the [supplementary material](#)]. On the contrary, the adsorption isotherms  $\Gamma_2^{(1)}$  and  $\Gamma_1^{(2)}$  of mixture C exhibit a minimum in the VL<sub>1</sub> and VL<sub>2</sub> regions, respectively [cf. Fig. 5(b) and the [supplementary material](#)]. In general, for the same mixture and temperature, the relative adsorption of component 1  $\Gamma_1^{(2)}$  exhibits an opposite behavior to  $\Gamma_2^{(1)}$  (cf. Fig. S7 in the [supplementary material](#)), which is as expected.

The relative adsorption  $\Gamma_2^{(1)}$  for mixture A and mixture B on the one hand and mixture C on the other hand shows important

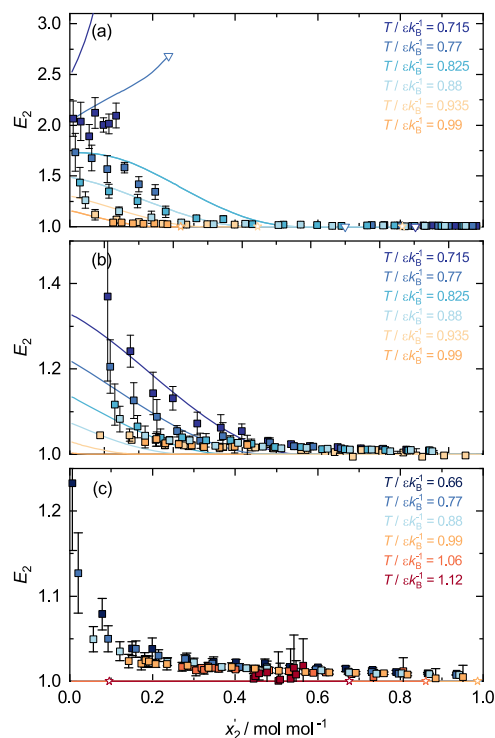
differences. These differences can also be seen in the corresponding density profiles (cf. Fig. 3). The differences are discussed here using the results for  $T = 0.88 \epsilon k_B^{-1}$ , as an example, where both components are subcritical. At  $T = 0.88 \epsilon k_B^{-1}$ , all three studied mixtures have VL<sub>1</sub> and VL<sub>2</sub> equilibrium regions that are connected at an azeotropic point [cf. Figs. 1(a)–1(c)]. Starting at infinite dilution of component 2, for mixture A and mixture B, a distinct enrichment peak in the interphase contributes to the relative adsorption  $\Gamma_2^{(1)}$  in the VL<sub>1</sub> region (cf. Fig. 3). The enrichment peak in the density profiles vanishes upon approaching the azeotropic condition with increasing  $x_2'$  (cf. Fig. 3). With further increasing  $x_2'$  and entering the VL<sub>2</sub> equilibrium region, the relative adsorption  $\Gamma_2^{(1)}$  becomes negative, which is due to a relative shift of the two component density profiles.<sup>11,20</sup> For mixture C on the other hand, no enrichment peak is observed. Hence, both the positive and negative relative adsorptions for mixture C are solely a result of a relative shift of the two component density profiles [cf. Figs. 3 and 5].

Overall, the results for the relative adsorption of component 1 with respect to component 2  $\Gamma_1^{(2)}$  have a complementary behavior to  $\Gamma_2^{(1)}$ . This is as expected since  $\Gamma_1^{(2)}$  and  $\Gamma_2^{(1)}$  are directly related by definition.<sup>16</sup> Yet, the results for  $\Gamma_1^{(2)}$  in combination with the underlying interfacial structure (cf. Fig. 3) yield some interesting findings: for mixture A, the positive relative adsorption of component 1  $\Gamma_1^{(2)}$  is based to some extent on an enrichment at the interface (cf. Fig. 3). For mixture B and mixture C, no enrichment of component 1 is observed in the entire composition and temperature range. Thus, the positive relative adsorption  $\Gamma_1^{(2)}$  observed for mixture B and mixture C (see the [supplementary material](#)) is solely a result of a relative shift of the two component density profiles. The negative adsorption, i.e., desorption, of component 1 at the interface on the other hand is for mixture A and mixture B to some extent as a result of an enrichment of component 2 displacing component 1 particles, whereas the negative adsorption observed for mixture C is solely a result of a relative shift of the component density profiles. All this shows that the interfacial structure is not uniquely characterized by the classical relative adsorption but should rather be discussed in the context and complementary to the enrichment behavior.

The adsorption isotherms for mixture A at  $T = 0.715 \epsilon k_B^{-1}$  and  $0.77 \epsilon k_B^{-1}$  are broken up, which is due to the heteroazeotrope [cf. Figs. 1(a) and 5(a)]. At the VL<sub>1</sub> interface, component 2 adsorbs and, vice versa, component 2 desorbs at the VL<sub>2</sub> interface. The large positive relative adsorption  $\Gamma_2^{(1)} > 0$  of component 2 at the VL<sub>1</sub> interface obtained for mixture A is a result of the strong enrichment of component 2 at the interface. In the direct vicinity of the three-phase equilibrium, the second liquid phase L<sub>2</sub> is built up in the VL<sub>1</sub> interface before reaching the VLLE. This can also be seen at mixture A's density profiles shown in Fig. 3 for the temperature  $T = 0.715 \epsilon k_B^{-1}$ .

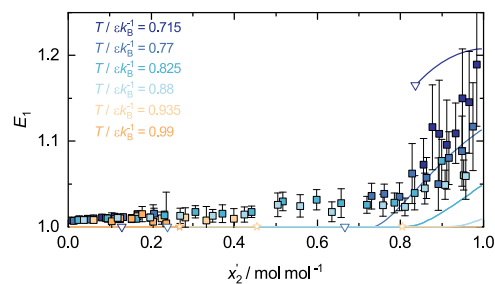
### 3. Enrichment

Figure 6 shows the results for the enrichment  $E_2$  of component 2 obtained from MD and DGT for all three mixtures. The results for the enrichment  $E_1$  of component 1 for mixture C are shown in Fig. 7. The corresponding  $E_1$  results for mixture A



**FIG. 6.** Enrichment  $E_2$  as a function of the liquid phase concentration  $x_2'$  for all studied temperatures and mixtures. Top to bottom are: mixture A, mixture B, and mixture C. Filled symbols represent data from MD simulations and lines predictions from DGT. In addition, the three-phase equilibrium ( $\nabla$ ) and the critical points ( $*$ ) obtained from the EOS are indicated. The DGT results shown in (c) coincide with the abscissa.

and mixture B are presented in the [supplementary material](#). The difference between the results obtained from MD and DGT is rather large in comparison to the surface tension and relative adsorption results discussed above. This is in line with results from previous studies.<sup>7,11,33,58</sup> These deviations between MD and DGT results for the enrichment can be attributed to two reasons: first, fluctuations present in profiles obtained from MD but not present in the



**FIG. 7.** Enrichment of component 1  $E_1$  as a function of the liquid phase concentration  $x_2'$  for mixture A. Filled symbols represent data from MD simulations and lines predictions from DGT. In addition, the three-phase equilibrium ( $\nabla$ ) and the critical points ( $*$ ) obtained from the EOS are indicated.

DGT profiles. By definition of the enrichment [cf. Eq. (11)], such fluctuations lead to an enrichment of component 2 larger than unity, which can be observed for most enrichment isotherms for mixture C [cf. Fig. 6(c)]. Second, deviations of the underlying thermodynamic models, i.e., the PeTS EOS and the LJTS force field, are probably the reason for a slight systematic overestimation of the DGT + EOS results observed for mixture A and mixture B for some isotherms.

For all studied temperatures of mixture B and all temperatures without a VLLE (i.e.,  $T/\epsilon k_B^{-1} = 0.825, 0.88, 0.935, 0.99$ ) of mixture A, the enrichment of component 2 exhibits a monotonic decay with increasing  $x_2'$  [cf. Figs. 6(a) and 6(b)]. This is the commonly reported behavior of the enrichment.<sup>11,58,63</sup> Moreover, for all studied cases, the enrichment of component 2 increases with decreasing temperatures, which is also in line with findings from the literature.<sup>1,7,63</sup>

An enrichment at a fluid interface is usually only observed for the low-boiling component 1.<sup>1</sup> This is not the case for mixture A as shown in Fig. 7. For the four lowest temperatures (i.e.,  $T/\epsilon k_B^{-1} = 0.715, 0.77, 0.825, 0.88$ ), an enrichment of component 1 is predicted for both MD and DGT (cf. Fig. 7). For all temperatures, the enrichment  $E_1$  is the highest at infinite dilution of component 1 and monotonically decreases with increasing mole fraction of component 1. This is in line with the established understanding of the enrichment of low-boiling components.<sup>1</sup> The enrichment of component 1 decreases with increasing temperature, which is also in accordance with the behavior of  $E_2$ . No significant enrichment  $E_1$  is observed for mixture B and mixture C (cf. Fig. S9 in the [supplementary material](#)).

For mixture A, the results obtained from MD and DGT show an enrichment of component 2 for the VL<sub>1</sub> interface. For the VL<sub>2</sub> interface, an enrichment of component 1 is observed (cf. Figs. 6 and 7). This change of the enriching component at the interface with varying composition can also be seen in the density profiles [cf. Fig. 3 (top, left)]. Overall, a picture evolves suggesting that, for mixture A, in each of the two vapor–liquid equilibrium regions VL<sub>1</sub> and VL<sub>2</sub>, respectively, the component enriches at the interface that effectively acts as the low-boiling component in that phase equilibrium region, which is mediated by the azeotropic point. Hence, the azeotropic point acts as a pseudo (high-boiling)-pure component.

Moreover, this interesting enrichment behavior contributes to the understanding of the relative adsorption behavior observed for mixture A [cf. Fig. 5(a)]; for the VL<sub>1</sub> equilibrium region, component 2 enriches at the interfaces, which leads to strong positive relative adsorption of component 2. Vice versa, for the VL<sub>2</sub> equilibrium region, component 1 enriches at the interface, which contributes to the negative relative adsorption of component 2.

In addition to the MD and DGT results, we applied the empirical enrichment model of Stephan and Hasse.<sup>1</sup> The empirical enrichment model was developed as  $E_2 = E_2(K_2^{5\%}, x_2', \Delta\rho_2)$ , where  $\Delta\rho_2$  is the density difference between the bulk phases. The model parameters were optimized to MD enrichment data of low-boiling components  $E_2$  for various binary LJTS mixtures.<sup>1</sup> Yet, we adopted the model straightforwardly for predicting  $E_1$  by using the model as  $E_1 = E_1(K_1^{5\%}, x_1', \Delta\rho_1)$ . The empirical model was applied for predicting  $E_2$  and  $E_1$  of all three mixtures in the entire composition and temperature range. The results are presented in the [supplementary material](#) in comparison to the MD data. Overall, the empirical model



is in excellent agreement with the MD reference data. It is also astonishing that the enrichment  $E_1$  is predicted very well by the empirical model.

### C. Interfacial properties along azeotropic line

Figure 8 shows the density profiles  $\rho_i$  with component  $i = 1, 2$  (left) and corresponding mole fraction profiles  $x_2$  (right) obtained from DGT at state points along the azeotropic line. Results for all three mixtures are shown. Figure 9 shows the interfacial properties (surface tension, relative adsorption of component 2, and interfacial thickness) derived from these profiles. At azeotropic points, the composition in the liquid phase is by definition equal to that in the vapor phase. Hence, the two components have no preferential residency in either of the two phases and the mixture along the azeotropic line can be considered as a pseudo-pure component. Yet, the total and partial density values of the two bulk phases at a given state point differ in general (cf. Fig. 8, left). With increasing temperature, the azeotropic line for the three mixtures (cf. Fig. 1) exhibits a monotonously increasing pressure. The azeotropic line ends for all three studied mixtures at high temperatures at a CAEP. More specifically, the azeotropic line has a similar shape as the pure component vapor pressure curves—for all three mixtures (cf. Fig. 1).

At the critical azeotropic endpoint, in addition to the equality of the composition of the two phases, also the densities of the two bulk phases become equal—as expected at a critical point. Hence, on an azeotropic line, the composition of the two bulk phases is equal throughout, and the densities of the two phases become equal upon approaching the CAEP. Therefore, an azeotropic line has several similarities to the pure component vapor pressure curves. The azeotropic composition does practically not vary with varying temperatures for all studied mixtures [cf. Figs. 1(a)–1(c)]. This can also be seen in the composition profiles shown in Fig. 8 (right): the mole fraction of component 2 of the vapor and liquid bulk phases slightly decreases with increasing temperature for mixture A and mixture B but slightly increases for mixture C. Interestingly, the azeotropic condition does not hold in the interphase, i.e., the composition profiles (cf. Fig. 8, right) are not constant in the interfacial region. Only upon approaching the CAEP, the composition of the interphase becomes equal to the composition of the two bulk phases.

No enrichment of component 2 and component 1 is observed on state points along the azeotropic line (cf. Fig. 8, left), i.e.,  $E_2 = 1$  and  $E_1 = 1$ . The surface tension  $\gamma$ , the relative adsorption of component 2  $\Gamma_2^{(1)}$ , and the interfacial thickness  $L_{10}^{90}$  at state points along

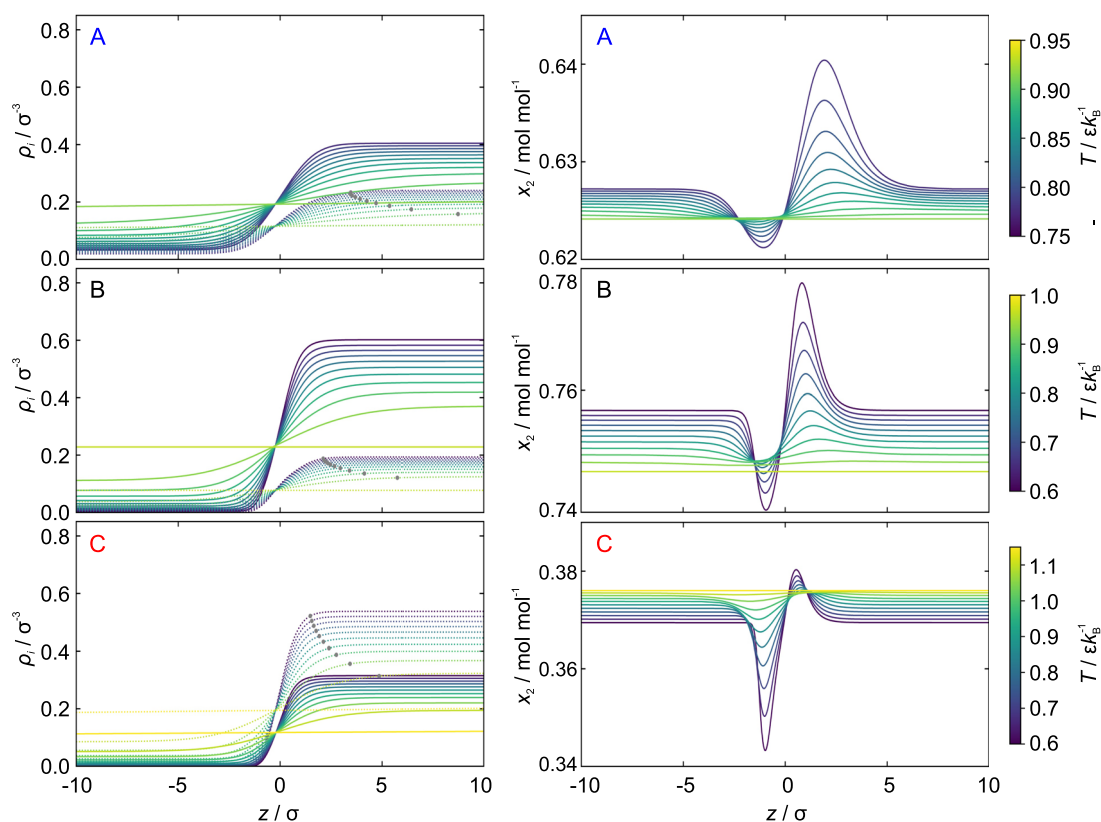


**FIG. 8.** Density profiles (left) and mole fraction profiles (right) obtained from DGT at state points along the azeotropic line (cf. green dashed line in Fig. 1). Results for mixture A (top), mixture B (middle), and mixture C (bottom). Dashed lines: high-boiling component 1; solid lines: low-boiling component 2. The color is coded by the temperature and the same for each row. The gray dots indicate the  $z$ -coordinate, where the density of component 1 reaches 97% of the corresponding liquid bulk value.



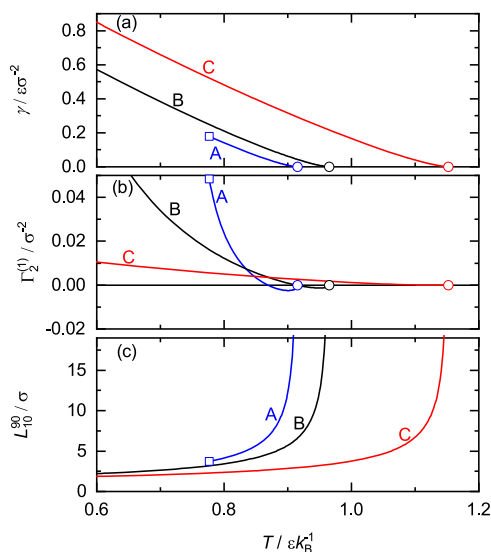


**FIG. 9.** Interfacial properties at state points along the azeotropic line (cf. green dashed line in Fig. 1) as a function of temperature. Results for mixture A (blue line), mixture B (black line), and mixture C (red line), obtained from DGT. (a) Surface tension  $\gamma$ , (b) relative adsorption  $\Gamma_2^{(1)}$ , and (c) interfacial thickness  $L_{10}^{90}$ . Open symbols represent the CAEP (○) and the HAEP (□).

the azeotropic line (cf. Fig. 9) provide further insights: the surface tension decreases monotonously for all three mixtures [cf. Fig. 9(a)]. This is as expected: the mixture behaves like a pseudo-pure component along the azeotropic line. Accordingly, the surface tension of that pseudo-component behaves like that of a pure component—it monotonously decreases and becomes zero at the critical azeotropic endpoint and the interfacial thickness exhibits a pole. This is further supported by the fact that the surface tension results along the azeotropic line for each mixture can be well described by the surface tension scaling law of a pure component,<sup>65,66</sup>

$$\gamma = \gamma_0 \left( 1 - \frac{T}{T_{\text{CAEP}}} \right)^{1.26}. \quad (13)$$

The adjustable parameter  $\gamma_0$  was obtained from a fit to the DGT surface tension results for each of the three mixtures. The obtained parameters are provided in the [supplementary material](#). The mean deviation of the DGT surface tension results along the azeotropic line and the surface tension correlation Eq. (13) is for all three mixtures below 0.3%. All of this support the picture that a fluid mixture along an azeotropic line can be considered as a pseudo-pure component.<sup>13,15,18</sup>

Here, we use the interfacial conformal solution theory<sup>20</sup> for discussing the azeotropic line interfacial property results of the three mixtures: the azeotropic pseudo-pure component has an increasing configurational internal energy with increasing  $\xi_{12}$ ,<sup>20</sup> which tightens the interface, i.e.,  $L_{90}^{10}$  decreases from mixture A to mixture B to mixture C at a given temperature [cf. Fig. 9(c)]. This picture is also in line with the behavior of the CAEP of the azeotropic pseudo-pure

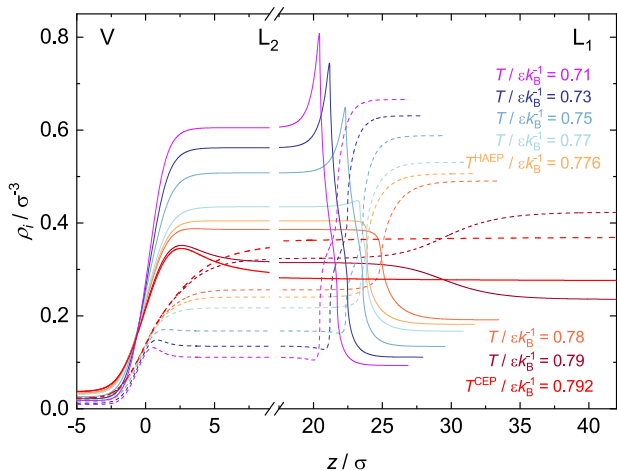
component [cf. Figs. 1(d)–1(f)], i.e., its temperature increases with increasing  $\xi_{12}$ , and a vapor–liquid equilibrium of the pseudo-pure component is stable at higher temperatures with increasing  $\xi_{12}$ . Moreover, the surface tension increases with increasing mean configurational internal energy by increasing  $\xi_{12}$  at a given temperature [cf. Fig. 9(a)], which is in line with predictions from the interfacial conformal solution theory.<sup>20</sup>

Figure 9(b) shows the relative adsorption of component 2 at the interface along the azeotropic line for the three studied mixtures. The relative adsorption of component 2 is zero for all mixtures at the corresponding CAEP. With decreasing temperature, the relative adsorption along the azeotropic line decreases first, before increasing to small positive values for all mixtures. The corresponding density profiles (cf. Fig. 8, left) reveal that the two component density profiles are only slightly shifted with respect to each other. Moreover, the azeotropic line density profiles yield no enrichment of either of the two components at the interface. These two facts (no relative shift of density profiles + no enrichment) result in the fact that the magnitude of the relative adsorption at the interface along the azeotropic line is very small: the absolute value of the relative adsorption along the azeotropic line is about an order of magnitude smaller than the relative adsorption observed in some fluid regions aside the azeotropic line (cf. Fig. 5). Yet, the relative adsorption along the azeotropic line is not zero [cf. Fig. 9(b)]. Hence, for the studied mixtures, the azeotropic line (where  $\Gamma_i^{(j)} = 0$ ) and the azeotropic line do not coincide. This is in line with observations from Refs. 9 and 13. The composition profiles further support this observation (cf. Fig. 8, right). For temperatures in the vicinity of the CAEP for a given mixture, the composition profiles are almost horizontal, which corresponds to very low relative adsorption [cf. Fig. 9(b)]. The composition profiles (cf. Fig. 8, right) reveal that, for all three mixtures, the low-boiling component 2 is slightly depleted at the vapor side of the interface and slightly aggregated at the liquid side of the interface.

#### D. Interfacial properties along VLE line

Figure 10 shows the density profiles at state points along the VLE line for mixture A obtained from DGT. Figure 11 shows the corresponding interfacial properties derived from these density profiles. Moreover, detailed isothermal phase diagrams in the vicinity of the VLE line are given in the [supplementary material](#). The VLE interfaces were computed in the entire temperature range where VLE exists [cf. Fig. 1(d)]. Moreover, the VLE interface was computed at two characteristic VLE points: the heteroazeotropic end point (HAEP) and the critical end point (CEP) [cf. Table I and Fig. 1(d)].

Along the VLE line, the three phases  $L_1$ ,  $L_2$ , and V coexist. Yet, only the phases  $L_1$  and  $L_2$  and the phases V and  $L_2$  are in direct contact for mixture A (cf. Fig. 10). The phases V and  $L_1$  are only indirectly connected with the phase  $L_2$  between them as a mediator. The surface tension  $\gamma$ , the enrichment of component 1  $E_1$ , and the enrichment of component 2  $E_2$  are reported in Fig. 11 for the three fluid interfaces, i.e.,  $VL_1$ ,  $VL_2$ , and  $L_1L_2$  (for the interface between  $VL_1$ , the phase  $L_2$  is considered a part of the interphase). The relative adsorption of component 2  $\Gamma_2^{(1)}$  and the interfacial thickness  $L_{90}^{10}$  are only reported for the interfaces between the phases  $VL_2$  and  $L_1L_2$ . For both properties  $\Gamma_2^{(1)}$  and  $L_{90}^{10}$ , no unambiguous values can



**FIG. 10.** Density profiles at state points along the VLE line for mixture A. Results from DGT. Dashed lines: high-boiling component 1; solid lines: low-boiling component 2. All interfaces exhibit an intermediate plateau at the second liquid  $L_2$  phase, which corresponds to a macroscopic film of  $L_2$  between the  $L_1$  and V phases.

be obtained for the interface between  $VL_1$  since the thickness, and thereby, also the relative adsorption depends on the film thickness of the equilibrium phase  $L_2$  that exists between the phase  $L_1$  and V (cf. Fig. 10).

The three surface tension values for the interface between  $VL_1$ ,  $VL_2$ , and  $L_1L_2$  at a given VLE state point are, in general, related by<sup>57,68</sup>

$$\gamma_{VL_1} \leq \gamma_{VL_2} + \gamma_{L_1L_2}, \quad (14)$$

where the equality indicates total wetting (layer of phase  $L_2$  between phase  $L_1$  and phase V) and the inequality indicates partial wetting (droplet of phase  $L_2$  between phase  $L_1$  and phase V).<sup>67–69</sup> For mixture A studied in this work, the left-hand-side and right-hand-side of the relation (14) are equal in the entire temperature range. Hence, DGT predicts total wetting along the entire VLE line for mixture A—as also found from the density profiles depicted in Fig. 10.

The interfacial properties along the VLE line (cf. Fig. 11) can be divided into two distinct temperature regimes: first, the regime of  $T < T^{\text{HAEP}}$  and, second, the regime  $T^{\text{HAEP}} < T < T^{\text{CEP}}$ . The second temperature regime is significantly shorter. Moreover, in the second temperature regime, the VLE line and the azeotropic line coincide in the pressure–temperature projection for the studied mixture A [cf. Fig. 1(d)]. In the second temperature regime, the  $VL_1$  equilibrium region (spanning from the first pure component to the azeotropic line) is attached to the miscibility gap, whereas the  $VL_2$  equilibrium region terminates in the azeotropic point (see the supplementary material for details). In the first temperature regime, on the other hand, both  $VL_1$  and  $VL_2$  regions terminate in the VLE.

At a given temperature at  $T < T^{\text{HAEP}}$ , the VLE and the azeotrope are effectively merged and a heteroazeotrope exists.

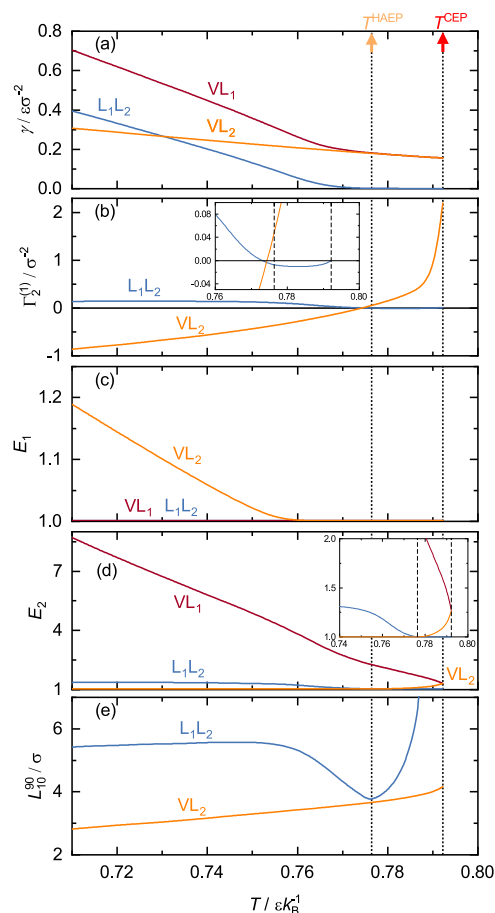


**FIG. 11.** Interfacial properties along the VLE line for mixture A (cf. red dotted line in Fig. 1) as a function of temperature. Results for the interface between the phases  $VL_1$  (dark red line),  $VL_2$  (orange line), and  $L_1L_2$  (blue line). Results obtained from DGT. (a) Surface tension  $\gamma$ , (b) relative adsorption  $\Gamma_2^{(1)}$ , (c) enrichment of component 1  $E_1$ , (d) enrichment of component 2  $E_2$ , and (e) interfacial thickness  $L_{90}^{10}$ . The temperatures of the HAEP and the CEP (cf. Table I) are indicated by the vertical dotted lines and arrows.

At the HAEP, the composition of the azeotrope is equal to the concentration of the phase  $L_2$  and the phase V (cf. Fig. S5 in the supplementary material). Moreover, the partition coefficient  $K_2$  of the  $L_1L_2$  and the  $VL_1$  regions is equal at the HAEP. In the temperature regime  $T^{\text{HAEP}} < T < T^{\text{CEP}}$ , the VLE is mainly connected to the  $VL_1$  equilibrium region; the  $VL_2$  equilibrium region is only connected to the VLE at the azeotropic point (see the supplementary material for details). Upon approaching the CEP, the  $L_1L_2$  equilibrium region at the VLE becomes narrow, i.e., the  $L_1$  and  $L_2$  phases become more alike, until they collapse in the critical end point and the  $L_1L_2$  region detaches from the  $VL_1$  region and the VLE vanishes.

The interfacial structure of the density profiles along the VLE line shows several interesting features (cf. Fig. 11): at low temperatures, a small enrichment of component 1 is observed at the  $VL_2$

interface. With increasing temperature, this enrichment decreases to unity at the HAEP [cf. Fig. 11(c)]. For the VL<sub>1</sub> interface (which comprises a layer of the equilibrium phase L<sub>2</sub>, cf. Fig. 10), a significant enrichment of component 2 is observed. The numbers for  $E_1$  at the VL<sub>2</sub> interface are significantly smaller than the numbers for  $E_2$  at the VL<sub>1</sub> interface at state points along the VLLE line [cf. Fig. 11(c)]. All this is fully in line with the findings for the enrichment behavior in the VL<sub>1</sub> and VL<sub>2</sub> regions (see above).

The interfacial VLLE structure provides further interesting insights: at low temperatures, a small depletion of component 1 at the L<sub>1</sub>L<sub>2</sub> interface is predicted by DGT (cf. Fig. 10). Simultaneously, an enrichment of component 2 is predicted at the L<sub>1</sub>L<sub>2</sub> interface. Furthermore, at high temperatures in the vicinity of the CEP, a small enrichment of component 2 is observed at the VL<sub>2</sub> interface, which becomes equal to  $E_2$  at the VL<sub>1</sub> interface [cf. Fig. 11(d)] as the two liquid phases fuse at  $T^{\text{CEP}}$ .

The two characteristic points HAEP and CEP have important consequences for the VLLE interfacial properties. Upon approaching the CEP, the L<sub>1</sub>L<sub>2</sub> interface becomes infinitely broad [cf. Figs. 10 and 11(e)]—as expected at a critical point. Accordingly, the L<sub>1</sub>L<sub>2</sub> surface tension becomes zero at the CEP [cf. Fig. 11(a)]. In addition, the relative adsorption of the L<sub>1</sub>L<sub>2</sub> interface becomes zero at the CEP [cf. Fig. 11(b)]. The enrichments  $E_1$  and  $E_2$  of the L<sub>1</sub>L<sub>2</sub> interface decay to unity at  $T^{\text{HAEP}}$  [cf. Figs. 11(c) and 11(d)].

At the HAEP, the VL<sub>2</sub> surface tension is equal to the surface tension value on the azeotropic line at the same temperature (cf. Fig. 9) since the VL<sub>2</sub> equilibrium at the VLLE at  $T = T^{\text{HAEP}}$  is also a part of the azeotropic line (see the [supplementary material](#) for details). For the same reason, the other interfacial properties of the VL<sub>2</sub> interface smoothly transition from the VLLE states to the azeotropic states in the temperature regime  $T^{\text{HAEP}} < T < T^{\text{CEP}}$ . Since the L<sub>1</sub>L<sub>2</sub> region vanishes upon approaching  $T^{\text{CEP}}$  and the two liquid phases L<sub>1</sub> and L<sub>2</sub> fuse to a single liquid phase, also the VL<sub>1</sub> surface tension converges to the VL<sub>2</sub> azeotropic surface tension value [cf. Fig. 11(a)].

The L<sub>1</sub>L<sub>2</sub> interface at VLLE conditions exhibits relatively low relative adsorption  $\Gamma_2^{(1)}$  as well as relatively low enrichment  $E_2$ . This is in line with a moderate enrichment obtained in the L<sub>1</sub>L<sub>2</sub> region besides the VLLE (see the [supplementary material](#)). The interfacial thickness of the L<sub>1</sub>L<sub>2</sub> interface, however, shows an interesting behavior: first, it is approximately constant in a wide temperature range. Then, with increasing temperature, the L<sub>1</sub>L<sub>2</sub> interfacial thickness drastically decreases and exhibits a minimum at  $T^{\text{HAEP}}$ .

#### IV. CONCLUSIONS

In this work, interfacial properties and phase equilibria of binary Lennard-Jones mixtures exhibiting different azeotropic phase behavior were investigated using both MD and DGT + EOS. For this purpose, three different mixtures were studied—each in a wide temperature range such that all relevant types of phase equilibria were covered by the study. The low-boiling component 2 and the high-boiling component 1 were the same for all mixtures. The binary interaction parameter was chosen such that mixture A and mixture B were of type II-A and mixture C of type I-A.

The complementary and well-validated approach<sup>7,11,20,33</sup> using both MD and DGT, as well as a suitable EOS for simple fluid

mixtures based on the Lennard-Jones truncated and shifted potential, enables the assessment of the relation of interfacial properties and characteristic phase equilibrium lines and points.

This work contributes to the understanding of the relation of fluid interfacial properties and the underlying phase equilibria of azeotropic mixtures. Different types of fluid phase equilibria and interfaces were studied: vapor–liquid, liquid–liquid, and vapor–liquid–liquid. The focus was on the vapor–liquid interfaces. Moreover, the relation of different interfacial properties and phase equilibrium properties was discussed in detail.

Overall, excellent agreement of the independent predictions from MD and DGT + EOS was obtained—for both the phase equilibrium and the interfacial properties. This is in line with previous studies of our group, which were based on the same approach.<sup>4,7,11,63</sup> Only for the enrichment, the interfacial thickness, and the phase equilibria in the vicinity of critical points obtained from the two methods, some systematic deviations are found, which have also been characterized before.<sup>7,11</sup>

Complex interfacial structures are obtained and elucidated for the three simple binary mixtures, e.g., a wetting transition, enrichment of both the high-boiling and low-boiling components, the composition and density profiles at azeotropic states, and the azeotropic behavior. Despite the fact that the three mixtures solely differ in the binary interaction parameter used in the Berthelot combination rule, the three mixtures exhibit completely different phase equilibria and interfacial properties. Most importantly, the three synthetic mixtures enable a systematic investigation of the interfacial excess at fluid interfaces in simple fluid mixtures: no enrichment is observed for high-boiling azeotropic mixtures (strong cross affinity of the two components); significant enrichment is observed for both component 2 and component 1 at low concentrations of the respective component for a heteroazeotropic mixture with very wide-boiling phase behavior (low cross affinity of the two components). The results from this work show that, in such a case, an enrichment of component 1 and component 2 can occur in the phase equilibrium branch where the respective component effectively acts as the low-boiling component mediated by an azeotropic point. For a low-boiling azeotropic mixture, an enrichment is only observed for the low-boiling component. All this is inherently covered by the very simple empirical enrichment model<sup>1</sup> based on the partition coefficient. Therefore, the empirical enrichment model developed for the prediction of the enrichment of a low-boiling component at a vapor–liquid interface can be straightforwardly applied to model the enrichment of both components in low-boiling azeotropic and high-boiling azeotropic mixtures as studied in this work.

As recently described for a type III phase behavior LJTS mixture,<sup>7</sup> also the heteroazeotropic type II-A phase behavior studied in this work shows a wetting transition: the second liquid phase L<sub>2</sub> starts forming under the influence of the gradients at the VL<sub>1</sub> interface before the VLLE is actually established. This goes in hand with a strong adsorption of component 2 and a strongly increasing interfacial thickness upon approaching the VLLE. Yet, it should be noted that the DGT predictions for the vapor–liquid density profiles in the vicinity of the VLLE yield extreme gradients, which is inherently problematic for the (square) gradient approximation. For future work, it would be interesting to study this wetting transition in more detail through molecular simulation computer experiments.

Interestingly, the concentration profiles across the interface for azeotropic states show a non-monotonic behavior in all studied cases. Hence, the azeotropic condition  $x'_2 = x''_2$  does not hold in the interphase, and a small relative adsorption is obtained for vapor–liquid interfaces at azeotropic state points.

It was furthermore shown that the conformal solution theory<sup>20</sup> can be favorably used to explain interfacial properties of simple fluid mixtures, e.g., the fact that interfacial properties along the azeotropic line can be considered as a pseudo-pure component.

## SUPPLEMENTARY MATERIAL

See the [supplementary material](#) for the numeric values for the MD and DGT data, which are reported there as an electronic spreadsheet. Furthermore, density profiles obtained from the MD simulations, the density profiles obtained from DGT for the LLE for mixture A, isothermal phase diagrams at state points along the VLE line of mixture A, as well as the results for the enrichment of the high-boiling component 1 for mixture B and mixture C, and the relative adsorption of low-boiling component 1 at the interface with respect to component 2 are shown. In addition, the invariant intersection points in the density profiles are discussed. Moreover, the results of the empirical enrichment model for  $E_1$  and  $E_2$  of Stephan and Hasse<sup>1</sup> are shown in comparison to the MD data.

## ACKNOWLEDGMENTS

The authors gratefully acknowledge funding of this work by the IRTG 2057 (Grant No. 252408385). The simulations were carried out on the ELWE supercomputer at Regional University Computing Center Kaiserslautern (RHRK) under the grant TUK-MTD. This research was conducted under the auspices of the Boltzmann-Zuse Society of Computational Molecular Engineering (BZS).

## AUTHOR DECLARATIONS

### Conflict of Interest

The authors have no conflicts to disclose.

### Author Contributions

J.S. and S.S. contributed equally to this work.

**Jens Staubach:** Conceptualization (equal). **Simon Stephan:** Conceptualization (equal).

## DATA AVAILABILITY

All primary data obtained from EOS + DGT and the MD simulations as well as the employed empirical model are provided in the [supplementary material](#) in a spreadsheet file. Furthermore, an explanation of that data is given in the [supplementary material](#) PDF file.

## REFERENCES

- 1 S. Stephan and H. Hasse, “Enrichment at vapour–liquid interfaces of mixtures: Establishing a link between nanoscopic and macroscopic properties,” *Int. Rev. Phys. Chem.* **39**, 319–349 (2020).
- 2 C. Klink and J. Gross, “A density functional theory for vapor–liquid interfaces of mixtures using the perturbed-chain polar statistical associating fluid theory equation of state,” *Ind. Eng. Chem. Res.* **53**, 6169 (2014).
- 3 R. Nagl, P. Zimmermann, and T. Zeiner, “Interfacial mass transfer in water–toluene systems,” *J. Chem. Eng. Data* **65**, 328–336 (2020).
- 4 S. Stephan, K. Langenbach, and H. Hasse, “Enrichment of components at vapour–liquid interfaces: A study by molecular simulation and density gradient theory,” *Chem. Eng. Trans.* **69**, 295–300 (2018).
- 5 S. Stephan, D. Schaefer, K. Langenbach, and H. Hasse, “Mass transfer through vapour–liquid interfaces: A molecular dynamics simulation study,” *Mol. Phys.* **119**, e1810798 (2021).
- 6 M. M. Telo da Gama and R. Evans, “The structure and surface tension of the liquid–vapour interface near the upper critical end point of a binary mixture of Lennard–Jones fluids. I. The two phase region,” *Mol. Phys.* **48**, 229–250 (1983).
- 7 S. Stephan and H. Hasse, “Interfacial properties of binary mixtures of simple fluids and their relation to the phase diagram,” *Phys. Chem. Chem. Phys.* **22**, 12544–12564 (2020).
- 8 A. H. Falls, L. E. Scriven, and H. T. Davis, “Adsorption, structure, and stress in binary interfaces,” *J. Chem. Phys.* **78**, 7300–7317 (1983).
- 9 W. A. Fouad and L. F. Vega, “The phase and interfacial properties of azeotropic refrigerants: The prediction of azeotropes from molecular theory,” *Phys. Chem. Chem. Phys.* **19**, 8977–8988 (2017).
- 10 E. Schäfer, G. Sadowski, and S. Enders, “Interfacial tension of binary mixtures exhibiting azeotropic behavior: Measurement and modeling with PCP–SAFT combined with density gradient theory,” *Fluid Phase Equilib.* **362**, 151–162 (2014).
- 11 S. Stephan, K. Langenbach, and H. Hasse, “Interfacial properties of binary Lennard–Jones mixtures by molecular simulations and density gradient theory,” *J. Chem. Phys.* **150**, 174704 (2019).
- 12 D. J. Lee, M. M. Telo da Gama, and K. E. Gubbins, “The vapour–liquid interface for a Lennard–Jones model of argon–krypton mixtures,” *Mol. Phys.* **53**, 1113–1130 (1984).
- 13 B. González–Barramuño, E. Cea–Klapp, I. Polishuk, R. I. Canales, H. Quinteros–Lama, and J. M. Garrido, “Interfacial properties of fluorinated (F)–gases in azeotropic condition,” *J. Mol. Liq.* **350**, 118604 (2022).
- 14 See [www.ddbst.com](http://www.ddbst.com) for Dortmund data bank; accessed October 2021.
- 15 J. S. Rowlinson and F. L. Swinton, *Liquids and Liquid Mixtures* (Butterworth, London, 1982).
- 16 R. Defay, I. Prigogine, A. Bellmans, and D. H. Everett, *Surface Tension and Adsorption* (Longmans, London, 1966).
- 17 I. A. McLure, B. Edmonds, and M. Lal, “Extremes in surface tension of fluorocarbon + hydrocarbon mixtures,” *Nat. Phys. Sci.* **241**, 71 (1973).
- 18 H. Segura, J. Wisniak, P. G. Toledo, and A. Mejía, “Prediction of azeotropic behavior using equation of state,” *Fluid Phase Equilib.* **166**, 141–162 (1999).
- 19 M. Heier, S. Stephan, J. Liu, W. G. Chapman, H. Hasse, and K. Langenbach, “Equation of state for the Lennard–Jones truncated and shifted fluid with a cut-off radius of  $2.5 \sigma$  based on perturbation theory and its applications to interfacial thermodynamics,” *Mol. Phys.* **116**, 2083–2094 (2018).
- 20 S. Stephan and H. Hasse, “Molecular interactions at vapor–liquid interfaces: Binary mixtures of simple fluids,” *Phys. Rev. E* **101**, 012802 (2020).
- 21 M. P. Lautenschlaeger and H. Hasse, “Transport properties of the Lennard–Jones truncated and shifted fluid from non-equilibrium molecular dynamics simulations,” *Fluid Phase Equilib.* **482**, 38–47 (2019).
- 22 S. Stephan, M. T. Horsch, J. Vrabec, and H. Hasse, “MolMod—An open access database of force fields for molecular simulations of fluids,” *Mol. Simul.* **45**, 806–814 (2019).
- 23 S. Stephan, M. Dyga, H. M. Urbassek, and H. Hasse, “The influence of lubrication and the solid–fluid interaction on thermodynamic properties in a nanoscopic scratching process,” *Langmuir* **35**, 16948–16960 (2019).
- 24 M. Horsch, H. Hasse, A. K. Shchekin, A. Agarwal, S. Eckelsbach, J. Vrabec, E. A. Müller, and G. Jackson, “Excess equimolar radius of liquid drops,” *Phys. Rev. E* **85**, 031605 (2012).
- 25 W. Eckhardt, A. Heinecke, R. Bader, M. Brehm, N. Hammer, H. Huber, H.-G. Kleinhenz, J. Vrabec, H. Hasse, M. Horsch, M. Bernreuther, C. W. Glass,



- C. Niethammer, A. Bode, and H.-J. Bungartz, "591 TFLOPS multi-trillion particles simulation on SuperMUC," in *Supercomputing* (Springer, Berlin, Heidelberg, 2013), pp. 1–12.
- <sup>26</sup>S. Stephan, M. P. Lautenschlaeger, I. A. Alhafez, M. T. Horsch, H. M. Urbassek, and H. Hasse, "Molecular dynamics simulation study of mechanical effects of lubrication on a nanoscale contact process," *Tribol. Lett.* **66**, 126 (2018).
- <sup>27</sup>M. P. Allen and D. J. Tildesley, *Computer Simulation of Liquids* (Oxford University Press, Oxford, 1989).
- <sup>28</sup>H. A. Lorentz, "Über die Anwendung des Satzes vom Virial in der kinetischen Theorie der Gase," *Ann. Phys.* **248**, 127–136 (1881).
- <sup>29</sup>D. Berthelot, "Sur le mélange des gaz," *C. R. Hebd. Seances Acad. Sci.* **126**, 1703–1706 (1898).
- <sup>30</sup>M. Heier, S. Stephan, F. Diewald, R. Müller, K. Langenbach, and H. Hasse, "Molecular dynamics study of wetting and adsorption of binary mixtures of the Lennard-Jones truncated and shifted fluid on a planar wall," *Langmuir* **37**, 7405–7419 (2021).
- <sup>31</sup>J. A. van Meel, A. J. Page, R. P. Sear, and D. Frenkel, "Two-step vapor-crystal nucleation close below triple point," *J. Chem. Phys.* **129**, 204505 (2008).
- <sup>32</sup>C. Niethammer, S. Becker, M. Bernreuther, M. Buchholz, W. Eckhardt, A. Heinicke, S. Werth, H.-J. Bungartz, C. W. Glass, H. Hasse, J. Vrabec, and M. Horsch, "Isl mardyn: The massively parallel molecular dynamics code for large systems," *J. Chem. Theory Comput.* **10**, 4455 (2014).
- <sup>33</sup>S. Stephan, J. Liu, K. Langenbach, W. G. Chapman, and H. Hasse, "Vapor-liquid interface of the Lennard-Jones truncated and shifted fluid: Comparison of molecular simulation, density gradient theory, and density functional theory," *J. Phys. Chem. C* **122**, 24705–24715 (2018).
- <sup>34</sup>T. W. Leland, P. S. Chappellear, and B. W. Gamson, "Prediction of vapor-liquid equilibria from corresponding states principle," *AIChE J.* **8**, 482–489 (1962).
- <sup>35</sup>T. W. Leland, J. S. Rowlinson, and G. A. Sather, "Statistical thermodynamics of mixtures of molecules of different sizes," *Trans. Faraday Soc.* **64**, 1447–1460 (1968).
- <sup>36</sup>S. Stephan and H. Hasse, "Influence of dispersive long-range interactions on properties of vapour-liquid equilibria and interfaces of binary Lennard-Jones mixtures," *Mol. Phys.* **118**, e1699185 (2020).
- <sup>37</sup>J. V. Sengers and J. M. H. L. Sengers, "Thermodynamic behavior of fluids near the critical point," *Annu. Rev. Phys. Chem.* **37**, 189–222 (1986).
- <sup>38</sup>M. E. Fisher, "Renormalization group theory: Its basis and formulation in statistical physics," *Rev. Mod. Phys.* **70**, 653–681 (1998).
- <sup>39</sup>S. B. Kiselev and J. F. Ely, "Crossover SAFT equation of state: Application for normal alkanes," *Ind. Eng. Chem. Res.* **38**, 4993–5004 (1999).
- <sup>40</sup>S. B. Kiselev and D. G. Friend, "Cubic crossover equation of state for mixtures," *Fluid Phase Equilib.* **162**, 51–82 (1999).
- <sup>41</sup>A. P. C. M. Vinhal, W. Yan, and G. M. Kontogeorgis, "Application of a crossover equation of state to describe phase equilibrium and critical properties of n-alkanes and methane/n-alkane mixtures," *J. Chem. Eng. Data* **63**, 981–993 (2018).
- <sup>42</sup>J. A. Barker and D. Henderson, "Perturbation theory and equation of state for fluids: The square-well potential," *J. Chem. Phys.* **47**, 2856–2861 (1967).
- <sup>43</sup>J. A. Barker and D. Henderson, "Theories of liquids," *Annu. Rev. Phys. Chem.* **23**, 439–484 (1972).
- <sup>44</sup>J. Gross and G. Sadowski, "Perturbed-chain SAFT: An equation of state based on a perturbation theory for chain molecules," *Ind. Eng. Chem. Res.* **40**, 1244 (2001).
- <sup>45</sup>S. Stephan, J. Staubach, and H. Hasse, "Review and comparison of equations of state for the Lennard-Jones fluid," *Fluid Phase Equilib.* **523**, 112772 (2020).
- <sup>46</sup>C. Miqueu, B. Mendiboure, A. Graciaa, and J. Lachaise, "Modelling of the surface tension of pure components with the gradient theory of fluid interfaces: A simple and accurate expression for the influence parameters," *Fluid Phase Equilib.* **207**, 225 (2003).
- <sup>47</sup>H. Kahl and S. Enders, "Interfacial properties of binary mixtures," *Phys. Chem. Chem. Phys.* **4**, 931–936 (2002).
- <sup>48</sup>P. M. W. Cornelisse, C. J. Peters, and J. de Swaan Arons, "Application of the Peng-Robinson equation of state to calculate interfacial tensions and profiles at vapour-liquid interfaces," *Fluid Phase Equilib.* **82**, 119–129 (1993).
- <sup>49</sup>J. D. van der Waals, "Thermodynamische Theorie der Kapillarität unter Voraussetzung stetiger Dichteänderung," *Z. Phys. Chem.* **13U**, 657 (1894).
- <sup>50</sup>J. W. Cahn and J. E. Hilliard, "Free energy of a nonuniform system. I. Interfacial free energy," *J. Chem. Phys.* **28**, 258 (1958).
- <sup>51</sup>C. Miqueu, B. Mendiboure, C. Graciaa, and J. Lachaise, "Modelling of the surface tension of binary and ternary mixtures with the gradient theory of fluid interfaces," *Fluid Phase Equilib.* **218**, 189–203 (2004).
- <sup>52</sup>J. Mairhofer and J. Gross, "Modeling of interfacial properties of multicomponent systems using density gradient theory and PCP-SAFT," *Fluid Phase Equilib.* **439**, 31 (2017).
- <sup>53</sup>E. A. Müller and A. Mejía, "Interfacial properties of selected binary mixtures containing n-alkanes," *Fluid Phase Equilib.* **282**, 68–81 (2009).
- <sup>54</sup>A. Mejía and H. Segura, "Interfacial behavior in type IV systems," *Int. J. Thermophys.* **25**, 1395–1414 (2004).
- <sup>55</sup>B. Carey, "The gradient theory of fluid interfaces," Ph.D. thesis, University of Minnesota, Minneapolis, 1979.
- <sup>56</sup>J. P. R. B. Walton, D. J. Tildesley, J. S. Rowlinson, and J. R. Henderson, "The pressure tensor at the planar surface of a liquid," *Mol. Phys.* **48**, 1357–1368 (1983).
- <sup>57</sup>J. G. Kirkwood and F. P. Buff, "The statistical mechanical theory of surface tension," *J. Chem. Phys.* **17**, 338–343 (1949).
- <sup>58</sup>S. Becker, S. Werth, M. Horsch, K. Langenbach, and H. Hasse, "Interfacial tension and adsorption in the binary system ethanol and carbon dioxide: Experiments, molecular simulation and density gradient theory," *Fluid Phase Equilib.* **427**, 476 (2016).
- <sup>59</sup>J. Lekner and J. R. Henderson, "Surface tension and energy of a classical liquid-vapour interface," *Mol. Phys.* **34**, 333–359 (1977).
- <sup>60</sup>P. H. van Konynenburg and R. L. Scott, "Critical lines and phase equilibria in binary van der Waals mixtures," *Philos. Trans. R. Soc. London, Ser. A* **298**, 495–540 (1980).
- <sup>61</sup>A. Mejía, J. C. Pàmies, D. Duque, H. Segura, and L. F. Vega, "Phase and interface behaviors in type-I and type-V Lennard-Jones mixtures: Theory and simulations," *J. Chem. Phys.* **123**, 034505 (2005).
- <sup>62</sup>V. Bongiorno and H. T. Davis, "Modified van der Waals theory of fluid interfaces," *Phys. Rev. A* **12**, 2213–2224 (1975).
- <sup>63</sup>S. Stephan, S. Becker, K. Langenbach, and H. Hasse, "Vapor-liquid interfacial properties of the binary system cyclohexane + CO<sub>2</sub>: Experiment, molecular simulation and density gradient theory," *Fluid Phase Equilib.* **518**, 112583 (2020).
- <sup>64</sup>P. M. W. Cornelisse, "The square gradient theory applied simultaneous modelling of interfacial tension and phase behaviour," Ph.D. thesis, Technische Universiteit Delft, 1997.
- <sup>65</sup>G. Galliero, "Surface tension of short flexible Lennard-Jones chains: Corresponding states behavior," *J. Chem. Phys.* **133**, 074705 (2010).
- <sup>66</sup>D. Broseta, Y. Meleán, and C. Miqueu, "Parachors of liquid/vapor systems: A set of critical amplitudes," *Fluid Phase Equilib.* **233**, 86–95 (2005).
- <sup>67</sup>J. S. Rowlinson and B. Widom, *Molecular Theory of Capillarity* (Dover Publications, New York, 1982).
- <sup>68</sup>J. W. Cahn, "Critical point wetting," *J. Chem. Phys.* **66**, 3667–3672 (1977).
- <sup>69</sup>M. M. Telo da Gama and R. Evans, "The structure and surface tension of the liquid-vapour interface near the upper critical end point of a binary mixture of Lennard-Jones fluids. II. The three phase region and the Cahn wetting transition," *Mol. Phys.* **48**, 251–266 (1983).
- <sup>70</sup>J. Vrabec, G. K. Kedia, G. Fuchs, and H. Hasse, "Comprehensive study of the vapour-liquid coexistence of the truncated and shifted Lennard-Jones fluid including planar and spherical interface properties," *Mol. Phys.* **104**, 1509 (2006).